High-Resolution Measurement of Contact Stresses and Friction in Indentation and Machining by Full-Field Photoelasticity

Jobin T. Mathews*, Harshit Chawla, Dinakar Sagapuram

Department of Industrial and Systems Engineering, Texas A&M University, College Station, TX 77843, USA

Abstract

An experimental study has been made of the sliding plastic contact in wedge indentation and machining of ductile metals. The use of full-field photoelasticity has allowed direct determination of interface pressure and shear stress distribution along the tool (indenter) and workpiece sliding contact at micron-scale resolution. Sapphire, a transparent photoelastic material that possesses sufficiently high hardness to indent and machine metals, is used as the tool material. It is shown that the Coulomb friction model applies only at the edges of the contact where the interface pressure falls below a certain value associated with the material's flow stress. Within the plastic contact zone, the mode of friction as well as the relationship between interface pressure and shear stress are very complex. In both cases, it is shown that shear stress neither remains constant nor varies in proportion to the pressure. It is proposed that the complex nature of friction and stress field at the sliding contact can be understood through simultaneous observations of the metal plastic flow at and near the interface. Using in situ measurements of the velocity field near the interface and local stress distribution at the contact from photoelasticity, friction contribution to the overall work is calculated and shown to be substantial (greater than one-third) in the case of machining. Keywords: friction, photoelasticity, cutting, indentation, plasticity, contact mechanics

*Corresponding author: Jobin T. Mathews, jobin@tamu.edu

1. Introduction

The interfacial conditions at the die and workpiece contact in metalworking processes such as wire drawing, thin strip rolling, and machining differ substantially from other engineering tribological contacts. In these processes, the interface pressures are high enough to cause bulk plastic flow in the workpiece and good surface conformity at the contact, i.e., the real area of contact approaches the apparent area of contact [1, 2]. Moreover, in many instances, there is relative sliding between the die and the workpiece. Thus, the situation may be described as a sliding plastic contact. Another important attribute of these contacts is that the plastic deformation of the workpiece can cause break-up of the original surface, resulting in virgin surfaces; an extreme case in this regard is machining where the surface that comes into contact with the cutting tool face is entirely new. This often results in a strong metal-to-metal contact that must be plastically sheared if sliding between the die and workpiece were to take place. Therefore, additional secondary plastic deformation can also occur at the sliding contact under certain situations.

It is generally believed that when the interface pressure $p \lesssim \sigma_f$ (σ_f being the flow stress of the workpiece), the interface shear stress τ varies proportionally with pressure [2], a condition similar to that encountered in other lightly-loaded tribological contacts (Coulomb friction). However, when τ reaches the shear flow stress of the material, the workpiece instead of sliding against the die face undergoes plastic shear. It should be also noted that the yield condition in the workpiece can be satisfied by various different combinations of stresses [3], therefore, the interface pressure can vary widely along the contact. Because the shear flow stress is independent of p, the friction coefficient μ (= τ/p) is not necessarily a constant but can take multiple values. In such cases, an exact description of the interfacial sliding friction, important from the standpoint of tool wear and fracture, can be developed only through local measurements of the interface stresses (normal and tangential) and their variation along the contact zone.

A somewhat unrelated area where the problem of sliding plastic contact is encountered is in indentation testing, a commonly used technique to determine the mechanical properties of materials. A special case that is particularly relevant is indentation with sharp indenters such as cones and wedges, where frictional effects can be important because of relative sliding (slip) between the indenter and workpiece. Beginning with Atkins and Tabor's work [4], sharp indentation has attracted attention because of its potential to extract the uniaxial plastic stress-strain relationship in metals. For example, in indentation with cones, the representative plastic strain is a function of the indenter angle. Thus, by using indenters with different apical angles and using empirical relationships between indentation hardness and the material's flow stress, it is possible to obtain the plastic stress-strain curve. Although it has been recognized that interfacial friction at the indenter-workpiece contact can impact the predicted stress-strain curve [5], friction is generally either ignored or modeled, without verification, using the Coulomb's law with a constant μ [6, 7].

The present study was undertaken to examine these assumptions through direct measurements of the interface pressure and shear stress distribution in sliding plastic contacts. In particular, we use the digital photoelasticity method to obtain full information about the contact stresses in two plane-strain problems (machining and wedge indentation) at high spatial resolution. An innovative aspect of our experiments is the use of sapphire as the tool/indenter material. Sapphire exhibits photoelastic properties while being sufficiently hard to machine and indent metals. The key aspects of the sliding contact are characterized and particular attention has been paid to contact regimes where the conventional laws of sliding friction break down.

2. Background

Various experimental techniques such as instrumented tools, moire technique, caustics, and photoelasticity have been used in the past to investigate stress distribution at die-metal contacts. Methods that involve placement of pins (instrumented with load cells) along the contact; deposition of pressure-sensitive film on the surface of the die; or placing a thin metallic sheet between the workpiece and die and then measuring the height to which the sheet is protruded into small holes drilled into the die to estimate contact pressure distribution have been discussed by Schey [2]. All of these methods require specially constructed dies, have limited resolution, and may further disturb the local frictional conditions at the contact. The transmission moire technique [8] was found to be a suitable method for characterizing stresses inside the die (tool) without interrupting the process, although the technique has somewhat limited stress sensitivity of about 1 MPa. Another

non-contact optical method that has been used to obtain contact stress distribution (both normal and tangential stresses) in problems such as strip rolling and plastic indentation by a cylindrical indenter is the method of reflected caustics [9, 10]. In this method, the contact stress distributions are represented by polynomial functions whose coefficients are determined in an inverse manner by utilizing data from the pseudocaustics in the vicinity of the contact zone. Both of these methods rely on the use of transparent plastics (usually epoxy or acrylic) as the die/tool material, which limits the choice of workpiece materials that can be studied to soft metals like lead.

A technique that overcomes this limitation and has been successfully applied to obtain stress distribution at the tool-chip interface in machining is the instrumented split-tool method [11–14]. This involves using a composite tool divided into two parts, with a small air gap between them, and recording the normal and tangential forces acting on one or both parts of the tool independently. Varying the location of the air gap along the contact zone results in one data point (normal and shear stress) along the contact. The stress "distribution" is then constructed by conducting several experiments (under identical process conditions) using composite tools with different air gap locations. Since there are no restrictions on the type of material that can be used for the tool, the method can be used to study contact conditions over a wide variety of tool/workpiece combinations. However, the drawbacks include the laborious nature of the experiments, and in the case of machining, difficulty of obtaining data close to the the cutting edge.

When compared to the above, photoelasticity [15, 16] has emerged as a powerful experimental technique to study contact stresses due to its unique combination of benefits that include high stress sensitivity, suitability for obtaining stress distribution data under realistic process conditions without the need for special dies and tools or disturbing the contact, and the ability to characterize stresses at improved spatial resolution. Some of the notable applications of photoelasticity in materials processing include the simulated wire drawing experiments through photoelastic die material [17]; estimation of stress distribution at the contact between metal and die in strip drawing [18, 19], rolling [20, 21] and backward extrusion [22]; and characterization of tool-chip contact stress distribution in machining [23–27]. Of these, machining has seen the most extensive application of photoelasticity, likely due to the critical role contact stresses play in determining tool wear

and breakage.

The earliest application of photoelasticity in machining involved the use of birefringent plastics pressed against specially designed models [23] and ready-made chips [28] to simulate the tool-chip contact. Later, photoelastic materials like epoxy and polycarbonate were utilized to reveal the tool-chip contact stress distribution during the actual machining process [24], although the use of plastic tools limited the choice of materials that can be machined; in most cases, only soft metals like lead could be investigated. Despite this limitation, the study by Usui and Takeyama [24] has provided valuable information about the distribution of normal and shear stresses along the tool-chip contact. The normal stress was found to increase towards the cutting tool tip with a plateau in the middle of the contact length, while the shear stress was found to be distributed uniformly over the contact length except near the chip separation point where a sharp stress decay was observed. The value of the uniform shear stress was found to be nearly equal to the shear yield strength of the material being machined, which suggested that the chip underside is plastically deformed as it slides past the tool face. The uniform distribution of shear stress along the tool-chip contact and its correlation with the material's shear strength was further supported by Chandrasekaran and Kapoor [25], who also investigated the effect of tool geometry (rake angle) on the stress distribution. However, in Chandrasekaran and Kapoor's study, the normal stress was found to continuously increase towards the cutting tool tip without a plateau. In contrast to these studies, a subsequent photoelastic investigation by Amini [26] suggested that shear stress along the contact is not constant but increases monotonically towards the tool tip.

Therefore, it can be seen that considerable confusion exists over the exact nature of tool-chip contact stress distribution. In addition, it must be noted that all the studies discussed above have relied on conventional photoelasticity, which results in sparse data. For example, the number of data points along the contact depends on the number of fringes that are present at the contact length, and determining the principal stress difference at these points requires as many images using the plane polariscope arrangement. Consequently, the data resolution along the contact is limited, which makes the characterization of stress components close to the tool tip – where steep stress gradients exist – a considerable challenge. This limitation led previous researchers to either

present no data near the tool tip or estimate stresses in this region based on the extrapolation of data away from the tool tip. The contradicting views regarding the tool-chip contact stress distribution are likely rooted in this issue.

The next major advance in the application of photoelasticity to sliding plastic contact problems, in particular machining, came from Bagchi et al. [29] who used sapphire as the cutting tool. The high hardness of sapphire enabled machining of harder materials such as steel, aluminum, and brass under realistic machining conditions. It was shown that the normal stress increases exponentially towards the cutting tool tip, while the shear stress exhibits a maximum roughly at the middle of the contact length before dropping to a small value near the tool tip. Bagchi et al. also used the conventional photoelasticity technique, and thus the data resolution was still limited to about 0.1 mm, similar to that in the previous studies [24–26]. Inspired by Bagchi et al., Barbat and Rao [30] also later used sapphire as the die material to analyze contact stresses in strip drawing. However, except for these studies, the use of sapphire to investigate contact stresses either in processing problems or indentation testing still remains largely unexplored. In fact, direct measurements of contact stress distribution in indentation appear to be rather rare. While some photoelastic investigations of the stress field in the indentation of elastic materials (e.g., elastomers, glasses) have appeared in the recent literature [31–33], similar studies focused on plastic indentation of metals do not exist to our knowledge. Also, in virtually every indentation analysis, frictional stress is either ignored or described using Coulomb's law.

This paper describes a study that was undertaken in the appraisal of the applicability of conventional laws of sliding friction to plastic contacts and to resolve some of the controversies related to the nature of contact stresses discussed above. We consider two problems – indentation with a sharp wedge and orthogonal plane-strain cutting. As in Bagchi et al.'s study, sapphire was used as the tool/indenter to characterize stress profiles at the contact. However, instead of using the conventional photoelasticity method, we use a phase-shifting technique to obtain full-field information of the stresses within the photoelastic tool and along the contact zone at micron-scale resolution not achieved previously. This improved resolution has proved critical for resolving steep stress gradients near the tool/indenter tip, where it is shown that the conventional laws of sliding break

down.

The remainder of the paper is organized as follows: an overview of the plastic flow and contact conditions in cutting and wedge indentation is provided in Sec 3. Section 4 provides details of the experimental setup used for photoelasticity measurements and the analysis techniques employed for quantifying stresses. The experimental results and validation of the technique are presented in Sec. 5. Implications of the findings and concluding remarks are discussed in Secs. 6 and 7, respectively.

3. Contact Mechanics of Cutting and Wedge Indentation

To illustrate the basic mechanics of plastic flow and the nature of sliding contact conditions in plane-strain cutting and wedge indentation, experiments were conducted where the metal specimen was observed in situ as it is machined or indented. Figures 1(a) and (b) show the schematic representations of the cutting and wedge indentation configurations, respectively. In these experiments, the tool was kept stationary and the workpiece was moved against the tool to replicate cutting and indentation. An optical high-speed camera (pco dimax HS4, integrated with a microscopic lens) with appropriate spatial and temporal resolution was used for in situ observation of the toolworkpiece contact zone. In the case of cutting, the images were obtained at a spatial resolution of 0.99 μ m/pixel with 0.5 ms inter-frame time, while in indentation, the spatial resolution was 1.98 μ m/pixel and the inter-frame time was 2 ms. The image sequence captured by the camera was subsequently analyzed using an image correlation technique called Particle Image Velocimetry (PIV) [34] to obtain full-field displacement data within the workpiece. In brief, PIV works on the principle of cross-correlation where we first identify a set of grid points in the image, define an interrogation window surrounding each point, and then calculate displacements at those points by performing cross-correlation between the interrogation windows of consecutive images. For more details of the PIV technique and its application to contact/plasticity problems, see Refs. [35, 36]. An experimental challenge in these studies is that they rely on observations made at the outer surface of the workpiece where ideal plane-strain conditions may not exist. This problem was overcome by lightly constraining the workpiece outer surface using a transparent glass plate (to prevent out-of-plane flow) and imaging the contact zone through the glass constraint.

The cutting process involves removing a thin layer of material from the workpiece surface in the form of a chip by the action of a hard wedge-shaped cutting tool. When the cutting edge is perpendicular to the relative tool-workpiece motion, and the cutting width large compared to the depth, a state of two-dimensional plane-strain deformation prevails during chip formation. The type of chip produced by cutting is sensitive to the workpiece material properties [37]. When machining ductile metals, a continuous ribbon-type chip is produced, and cutting under these conditions can be described as a steady-state process. As an example, Fig. 2 shows chip formation in cutting of a ductile brass workpiece, where four images taken at different time instances of the cutting process are presented. A virtual grid is superimposed on image 1, which is then tracked in subsequent images using the displacement field obtained from PIV. Observation of the grid reveals that the material experiences large plastic shear as it enters the primary deformation zone (region OA in Fig. 2) and becomes part of the chip. Importantly, the deformation/flow pattern is identical at all times, indicating the steady-state nature of the cutting process. As will be shown later, this feature simplifies the experimental needs for photoelasticity measurements since the steady state allows for acquisition of multiple "snapshots" of the cutting process without interrupting the test.

From Fig. 2, it can be also seen that the chip makes contact with the tool rake face over some finite distance (marked by region OB in the figure) and flows past the tool face as new incoming material enters the primary deformation zone. When compared to other tribological contacts, the local conditions at the tool-chip interface are somewhat unique, in that not only the real and apparent areas of contact are equal due to high pressures at this contact but also the newly generated chip underside in contact with the tool is intrinsically clean (i.e., devoid of oxide layer or contaminants). These conditions often result in additional secondary deformation in the chip locally at the sliding contact. This can be for instance seen in Fig. 2 where the yellow lines, while being straight in the chip, bend (deform) near the tool-chip contact as the chip slides past the tool rake face.

Additional details of the tool-chip sliding contact are provided in Fig. 3. Figure 3(a) for example shows the velocity distribution in cutting, where a local gradient in the velocity at the tool-chip

contact is evident. This local velocity gradient at the contact can be clearly understood from the velocity profiles shown in Fig. 3(b), where the chip velocity near the interface is plotted as a function of distance from the tool tip (x). The individual curves shown in different colors correspond to material layers located at different normal distances (y) from the tool rake face. It can be seen that the material away from the interface (yellow, green, and black curves, Fig. 3(b)) moves at a constant velocity, while material layers (blue and red) adjoining the interface flow at a lower velocity. This retardation of material flow at the tool-chip interface has been previously likened to the boundary layer phenomenon in viscous fluids [38], although it is important to note that chip velocity at the interface (y=0) is not zero. Thus, both sliding and subsurface plastic deformation in the chip occur simultaneously.

The plastic flow field and contact conditions in indentation with a sharp wedge (60° included angle) were studied using the same technique and these observations are summarized in Figs. 4 and 5. Unlike cutting, indentation is a non-steady process, that is, stress and strain at a fixed point vary throughout the process. However, wedge indentation falls under a special class of non-steady problems where the plastic deformation zone develops in a geometrically similar manner [39]. This can be seen from the grid maps in Fig. 4 where snapshots of the deformation field at different indentation depths (t_0) are shown. It is observed that regardless of t_0 , the plastic zone takes the form of semi-circular loops located symmetrically on both sides of the indenter. During indentation, the plastic zone expands in proportion to t_0 ; therefore, if the geometry is scaled with respect to t_0 , the plastic zone remains the same at all times. This geometric similarity means that measurements made at one indentation depth are applicable to all depths, a feature that we exploit in our photoelasticity measurements (see Sec. 5.2).

Another notable feature of indentation with a sharp wedge is the mode of material flow around the indenter tip that has been termed "cutting" [40–42]. This deformation mode can be understood by tracking the specimen's top surface marked by the red line in Fig. 4. It can be seen that the line does not remain continuous but is cut by the tip of the indenter. For example, if we consider two neighboring material elements A and A' that are initially located at the indenter tip, it can be seen that after indentation, they no longer remain immediate neighbors but end up about midway

of the contact length on either side of the indenter because of the cutting deformation mode. It happens that during plastic indentation, two processes simultaneously occur at the indenter face – new material elements from the specimen's top (original) surface come into contact with the indenter (demarcated by the red line in contact with the indenter face, Fig. 4), while the indenter face closer to the tip is exposed to new material that was initially located in the interior of the specimen. The result is that regardless of the indentation depth, the indenter face is simultaneously in contact with both the original surface and the newly created (virgin) surface.

Inspection of the velocity field in indentation in Fig. 5(a) shows that sliding at the indenter-workpiece contact is relatively uniform along the entire contact. Also, see Fig. 5(b) that shows the velocity profile along the contact; as before, the profiles are plotted for different material layers parallel to the indenter face but located at different normal distances (y). It is evident that except near the free surface, the sliding velocity is uniform along the contact. Moreover, no velocity gradient along the normal direction was found, which is in contrast to that observed for the tool-chip contact in cutting. Taken together, the contact conditions in both the problems, while sharing certain common characteristics (both are sliding plastic contacts), show sufficient differences to warrant separate investigations.

4. Experimental

This section presents experimental details related to characterization of contact stresses using the photoelasticity technique. The use of photoelasticity to characterize stresses requires a birefringent tool material that possesses a high hardness comparable to that of commercial tools and indenters. Sapphire, a single crystal form of Al_2O_3 , which satisfies both the requirements was used as the tool material. This is coupled with a phase-shifting technique to obtain full-field stress data within and along the contact of the tool/indenter.

4.1. Experimental arrangement

Photoelasticity is based on the property of temporary stress-induced birefringence. The technique uses an experimental arrangement called polariscope, involving polarizers and quarter-wave plates. As the polarized light passes through a photoelastic material, the principal stress directions

at any given point act as polarizing axes, and the two refracted rays travel at different velocities, causing relative retardation. This results in two different types of fringes – isoclinics and isochromatics. Isoclinics appear when the principal stress direction at a point coincides with the polarization direction of the plane-polarized light. Thus, the isoclinic fringe corresponds to the principal stress direction. The isochromatic fringes occur due to the retardation and therefore provide information about the principal stress difference. The isochromatic fringes appear as dark and bright fringes when the light source is monochromatic, and colored when the light source is white light. In contrast, the isoclinic fringes remain black for any light source. A plane polariscope arrangement (using the arrangement: light source/polarizer/photoelastic model/analyzer), gives both isoclinic and isochromatic fringes. However, using a circular polariscope arrangement (using the arrangement: light source/polarizer/quarter wave plate/photoelastic model/quarter wave plate/analyzer), isoclinics can be removed, giving only isochromatic fringes. Both of these configurations were used together to obtain full-field isoclinic and isochromatic parameter information.

The experimental configuration developed to study contact stress distribution in cutting and wedge indentation is shown in Fig. 6. The photoelastic model, which in our case is the sapphire cutting tool or indenter, was kept stationary with respect to the optical elements, light source, and camera. For cutting experiments, a special tool holder was designed to hold the sapphire cutting tool, and chip formation was effected by translating a rectangular workpiece against the stationary tool at a predefined cutting depth (t_0) and speed (V_0) . The reaction forces on the tool during the cutting process were measured in two orthogonal directions using a multi-component piezoelectric dynamometer (Kistler 9129AA model) mounted directly behind the tool. The wedge indentation experiments were performed on a MTS uniaxial testing machine. In these experiments, the workpiece was stationary and the indenter was moved with respect to the workpiece at a constant speed; only the normal load along the indentation axis was recorded in the indentation experiments.

The workpiece material studied was single-phase brass 260 (approximately 70% Cu - 30% Zn, by wt.%) with an initial Vickers hardness of 153 HV. The workpiece width (w) to cutting or indentation depth (t_0) ratio was kept sufficiently large to minimize the effect of non-plane-strain

conditions at the specimen edges. The w/t_0 ratio in cutting was about 50, while in indentation, the width to final indentation ratio was in the 4-15 range. In all the experiments, the tool/indenter width was 5% larger than the workpiece width to account for any lateral flow of material (along the width direction) in the vicinity of the contact zone.

A color camera (Apex AP-3200T-USB) was used for capturing the isoclinics and isochromatics during the experiments. It is important to note that the length of the contact zone in a typical cutting or an indentation experiment is of the order of 0.5-1 mm. Thus, our region of interest is very small. To obtain data at sufficient resolution, the camera was fitted with a $5 \times$ microscopic objective; this provided a field of view of 1.6 mm \times 2.1 mm at 1.03 μ m/pixel resolution. The use of objective lenses however limits the working distance available to accommodate the optical elements required for photoelasticity measurements. To address this issue, an in-house miniature polariscope, consisting of a white LED light source, polarizer (LPVISE100-A - \emptyset 1" Linear Polarizer), quarter wave plates (WPQ10E-633 - \emptyset 1" Polymer Zero-Order Quarter-Wave Plate), and an analyzer was developed and used this work, see Fig. 6. The polariscope was built using rotation mounts to facilitate manual rotation of the optical elements.

4.2. Calibration of sapphire's stress fringe coefficient (f_{σ})

Sapphire has a hexagonal crystal structure where every axis other than the optical axis (c-axis) has a natural birefringence. For this reason, all tools were prepared such that the c-axis of the tool coincides with the direction of light propagation. This ensures that only stress-induced birefringence effects due to mechanical loading are captured. Circular sapphire windows (optical grade, with impurity levels less than 2 ppm and surface roughness (R_a) of 0.004 μ m) of different thicknesses were procured from Meller Optics, Inc. and subsequently ground and lapped to produce the desired tool/indenter geometry. This included a rough cut to an approximate shape, followed by polishing on a faceting machine using diamond wheels of various grit sizes. After the final polishing step, the tool face had an R_a value of 0.25 μ m. The tool/indenter tip radius was about 5 μ m.

Quantitative stress analysis using photoelasticity requires information about the tool material's stress fringe value (f_{σ}) , a material constant that relates the optical data to mechanical stresses.

This material constant was determined by elastically deforming a sapphire specimen by applying a line load normal to its surface and comparing the fringe data with Flamant's analytical solution [43]. Flamant's solution for a line load applied normal to the surface of an elastic half-space predicts a simple radial stress distribution. In a polar coordinate system represented by r and θ' centered at the point of loading, the stress components $\sigma_{\theta'\theta'}$ and $\tau_{r\theta'}$ are zero, and the radial stress is given by:

$$\sigma_{rr} = \frac{2P'}{\pi} \frac{\cos \theta'}{r},\tag{1}$$

where P' represents the magnitude of line load, which is the total load (P) divided by width. To simulate this loading in actual experiments, a 3 mm thick sapphire plate (25 mm \times 25 mm in other dimensions) was elastically indented with a sharp high-speed steel wedge. The loading was performed in such a way that the wedge tip made uniform line contact over the entire thickness of the sapphire plate. The maximum indentation load was kept below 1,200 N to avoid any plastic flow or fracture. The sapphire plate indented to various loads below this value was observed using the same polariscope arrangement described earlier in Sec. 4.1 to characterize the fringes. As expected, a circular fringe pattern with the fringe order increasing towards the point of loading was observed. Now representing any fringe's diameter d in terms of the polar coordinates as $d = r/\cos\theta'$, Eq. 1 can be rewritten as:

$$\sigma_{rr} = \frac{2P'}{\pi d}.\tag{2}$$

The stress optic law, which relates the fringe order (N) and stress data at any point is given by:

$$\sigma_1 - \sigma_2 = \frac{Nf_\sigma}{w},\tag{3}$$

where σ_1 and σ_2 are the principal stresses and w is the specimen width. Note that for our problem,

 $\sigma_1 = \sigma_{rr}$ and $\sigma_2 = \sigma_{\theta'\theta'} = 0$. Therefore, combining Eqs. 2 and 3, we get an equation for f_{σ} :

$$f_{\sigma} = \frac{2P'w}{\pi dN} = \frac{2P}{\pi dN},\tag{4}$$

where d is the diameter of the N^{th} fringe. Figure 7(a) shows the experimental data for d for N=2 plotted as a function of the applied load P. As can be seen, the fringe diameter d increases linearly with P, as predicted by Eq. 4. The slope of this line gives the material stress fringe value for sapphire, which was found to be 383 N/mm/fringe. To further verify that the estimated f_{σ} value is correct, the experimental fringes were compared with the fringes obtained using the Flamant's analytical solution, see Fig. 7(b). The experimental image on the left in Fig. 7(b) was acquired using the dark-field circular polariscope arrangement. To obtain the corresponding reconstructed image using the Flamant's solution, the fringe order (N) at each point was estimated using the stress optics law (Eq. 3), which in turn gives the isochromatic parameter $\delta = 2\pi N$. The dark-field isochromatic fringes were then reconstructed using the intensity equation (I_6 in Table 1), which are shown in the image on the right in Fig. 7(b). An excellent match between the experimental and calculated fringes is evident, which provides validation both for the use of Flamant's solution and the estimated f_{σ} value.

4.3. Full-field analysis of stresses using digital photoelasticity

Conventional photoelasticity provides information about the fringe order and principal stress direction only along the isochromatic/isoclinic fringes. Obtaining this information over the entire field requires the use of special phase-shifting techniques (PST). Various phase-shifting techniques (PST) that have been proposed to obtain continuous full-field data for the fringe order (isochromatic) and principal stress direction (isoclinic) have been reviewed by Ramesh [44]. In this study, we use the ten-step phase shifting technique [45, 46], along with an adaptive quality-guided phase unwrapping (AQGPU) algorithm [47], on account of its accuracy and minimal influence of quarter wave plate mismatch error. Table 1 lists the optical arrangements and the respective intensity equations of the ten-step PST. The first four configurations correspond to the plane polariscope arrangement used for isoclinic parameter estimation, and the next six correspond to the circular

polariscope arrangement used for isochromatic parameter estimation. A challenge in phase-shifting techniques is that some errors can creep in due to quarter wave plate mismatch and isochromatic-isoclinic interaction. The use of the above ten-step method, with four plane polariscope images dedicated for isoclinic parameter estimation, eliminates the wave plate mismatch error, while the use of white light and color camera eliminates isoclinic-isochromatic interaction and allows accurate estimation of principal stress directions. The wrapped isoclinic parameter θ_w , which represents the direction of principal stresses, can be calculated from the first four intensity equations as:

$$\theta_w = \frac{1}{4} \tan^{-1} \left(\frac{I_4 - I_2}{I_3 - I_1} \right). \tag{5}$$

where θ_w can represent both the principal stress directions. To obtain an isoclinic phase map free of inconsistent zones, AQGPU algorithm [47] was used to unwrap the isoclinic data. Using this unwrapped isoclinic data (θ), isochromatic data free of the ambiguous zone was obtained. The isochromatic parameter, calculated from the other six intensity equations, is given by:

$$\delta_w = \tan^{-1} \left(\frac{(I_9 - I_7)\sin 2\theta + (I_8 - I_{10})\cos 2\theta}{(I_5 - I_6)} \right).$$
 (6)

where δ_w represents fractional retardation. This isochromatic data was further unwrapped (δ) and used to obtain the continuous fringe order as follows:

$$N = \frac{\delta}{2\pi}.\tag{7}$$

This information of the fringe order at all points was then used to obtain full-field principal stress difference data using the stress optic law (Eq. 3). Thus, using the phase-shifting technique, principal stress difference and principal stress directions (θ) at every point ("pixel") in the domain can be obtained.

Quantitative analysis of friction at the tool-workpiece contact requires the estimation of normal and tangential stresses along the contact. While full-field distribution of principal stress difference and principal stress direction can be obtained using digital photoelasticity and phase-shifting tech-

niques, they by themselves cannot provide direct information about the magnitude of stresses. Although principal stress difference and/or principal stress direction information is sufficient in many applications such as fracture mechanics (e.g., to calculate stress intensity factor [46, 48]) and validation of numerical models, determination of normal and tangential stresses along the frictional sliding contact requires knowledge of the complete stress tensor at all points along the contact zone. Techniques for estimating stresses from the photoelasticity data include the oblique-incidence method, interferometric method, hole method, and shear difference technique; see Ref. [49] for a detailed review of the currently available stress separation techniques. Of these, the interferometric technique involves the estimation of isopachic contours $(\sigma_1 + \sigma_2)$ and requires the incorporation of additional optical elements in addition to the polariscope, which is challenging in our case because of the space restrictions (limited working distance) noted earlier. In contrast, the oblique incidence method does not involve any modifications to the polariscope arrangement but requires the photoelastic material (tool/indenter) to have the same birefringence properties along multiple crystal axes; as a result, sapphire is not suitable for this method.

For these reasons, the shear difference technique [15] was used in this study. In this method, we start with a "seed" point where complete stress information is known, and the individual stress components over the domain of interest are then solved using a numerical marching scheme. In this work, Tesar's modified shear difference equation [50] is used, where the individual stress components are given by

$$\sigma_{xx}^{j} = \sigma_{xx}^{i} - \sum_{i}^{j} \frac{\Delta(\sigma_{1} - \sigma_{2})}{\Delta y} \frac{\sin 2\theta}{2} \Delta x - \sum_{i}^{j} (\sigma_{1} - \sigma_{2}) \cos 2\theta \frac{\Delta \theta}{\Delta y} \Delta x, \tag{8}$$

$$\sigma_{yy}^{j} = \sigma_{yy}^{i} - \sum_{i}^{j} \frac{\Delta(\sigma_{1} - \sigma_{2})}{\Delta x} \frac{\sin 2\theta}{2} \Delta y - \sum_{i}^{j} (\sigma_{1} - \sigma_{2}) \cos 2\theta \frac{\Delta \theta}{\Delta x} \Delta y, \tag{9}$$

where j is the point where stresses are unknown and need to be determined, while i represents the seed point. The shear stress τ_{xy} over the entire domain can be obtained using $\tau_{xy} = \frac{\sigma_1 - \sigma_2}{2} \sin 2\theta$. For the cutting problem, a point on the tool flank surface (see Fig. 2) away from the tool tip where the normal and shear stresses are zero (free surface) was used as a seed point. In the case of indentation, a point on the indenter face away from the contact zone similarly played the role

of a seed point. Once σ_{xx} and σ_{yy} are determined along a series of points, these points then act as the seed points for the algorithm to march along the x- and y-axes, thus providing full-field data for the stress components.

5. Results

In this section, results from our high-resolution photoelasticity measurements of contact stress distributions in indentation and cutting are presented. In addition to providing a quantitative measure of friction and its variation along the tool-workpiece contact, the results also demonstrate the steady-state (cutting) and geometric similarity (wedge indentation) nature of the problems studied.

5.1. Cutting

Figure 8 shows the fringe pattern in the cutting tool as viewed using circularly polarized light such that only isochromatics are visible, without the isoclinics. In the figure, four bright-field circular polariscope images captured at different time instances of the cutting process are shown. As can be seen, the fringe order increases towards the tool-chip contact, with the fringes centered on the rake face at a point located at a small distance from the tool tip. Importantly, the figure also shows that the fringes remain identical throughout the cutting process despite the dynamic nature of tool-chip contact in machining. As discussed earlier in Sec. 3, the tool-chip contact conditions are such that the virgin surface, generated by cutting action at the tool tip, continuously comes into contact with the tool face while some material points on the chip underside leave contact with the tool at the edge of the contact. The stationary fringes mean that these two processes are in "dynamic equilibrium" such that they do not lead to significant temporal variations in the overall stress distribution at the contact. Figure 8 also shows the evolution of cutting (F_C) and thrust (F_T) forces as the workpiece engages with the tool, produces a chip, and travels past the tool. F_C is the horizontal force component parallel to the V_0 direction, while F_T is the vertical force component acting normal to the machined surface. As can be seen, following an initial rise corresponding to incipient stages of chip formation (first 5 seconds), the forces essentially remain constant (within 5% of the mean value) during the cutting process, until the 37 second mark corresponding to tool disengagement from the workpiece. The constant force profiles together with the stationary fringes confirms the steady-state nature of the cutting process. An implication of the steady state observation is that multiple images with different optical arrangements required for photoelasticity analysis can be acquired at different time instances without interrupting the cutting process.

Taking advantage of the steady state observation, experiments were conducted at a relatively low cutting speed of 0.5 mm/s, which provided sufficient time to capture multiple images as per the ten-step PST (Table 1). In these experiments, the rotation of the optical elements to different orientations was performed manually. The first four steps in the ten-step PST correspond to the plane polariscope arrangement. Figure 9 shows the four images obtained using the first four optical arrangements, having only the polarizer and the analyzer, which are always kept crossed and rotated in unison in increments of 22.5°. As can be seen, the isochromatic fringes remain identical in the four images, while the isoclinics location is changed with the polariscope arrangement. Similarly, six images corresponding to steps 5-10 in the ten-step PST were obtained using the circular polariscope arrangement, as shown in Figure 10. Note that the first two images (steps 5 and 6) are respectively the bright-field and dark-field circular polariscope images.

The first four images (Fig. 9), together with the AQGPU algorithm, were used to obtain full-field isoclinic parameter data. All three channels (R, G, and B) in the four color images were used in the full-field isoclinic parameter estimation. The six images captured using the circular polariscope arrangement (Fig. 10) and the isoclinic data together were then used to obtain the wrapped isochromatic parameter; the wrapped isochromatic data was subsequently unwrapped using the AQGPU algorithm to obtain the full-field fringe order. Only the red channel in the color images was used in the isochromatic parameter estimation. Figure 11 shows the full-field wrapped and unwrapped isoclinic and isochromatic data thus obtained. In the unwrapped isoclinic plot shown in Fig. 11 (c), θ represents the direction of the principal stress measured counter-clockwise with respect to the horizontal direction. Before using this data for estimating stresses, a check was made on the isoclinic and isochromatic data for correctness. For this, both the full-field data were compared with the experimental images to check for accuracy at the fringes. For example, the center of the isochromatic fringes (location of minimum intensity) in dark- and bright-field circular

polariscope images must be integer fringe orders and odd multiples of half-integer, respectively. Similarly, θ at isoclinic fringes should match the orientation of the analyzer. In addition, the isoclinic data was checked for correctness of θ at the tool's free surface away from the contact zone (see points labeled A and B in Fig. 11), where the principal stress directions are known. These analyses validated the full-field isoclinic and isochromatic data and showed that the mean absolute percentage deviation (MAPE) for both the isoclinic and isochromatic parameters was less than 3%. The isoclinic and isochromatic data were then analyzed using the shear difference technique to obtain full-field information about the individual stress components over the tool.

Figure 12 shows the stress maps for σ_{xx} , σ_{yy} , τ_{xy} and σ_h (hydrostatis stress or mean of principal stresses). Here, x and y represent directions parallel and normal to the tool rake face, respectively. Therefore, σ_{yy} is the stress component acting normal to the rake face, while τ_{xy} is the shear stress along the rake face. Also, in our convention, negative values for σ_{xx} , σ_{yy} and σ_h mean that the stresses are compressive, while negative τ_{xy} means clockwise shear. As can be seen from the figure, the stress state near the tool tip is highly compressive, with the normal stress σ_{yy} showing a maximum at the tool tip (Fig. 12(b)). Shear stress (τ_{xy}) distribution along the tool-chip contact, on the other hand, exhibits a maximum not at the tool tip but at a small distance away from the tip (Fig. 12(c)). The stress maps also reveal that the tool flank face (relief face adjacent to the machined surface) is not entirely stress-free, but there exists a finite contact zone near the tool tip over which the machined surface rubs against the tool flank face. This, for instance, can be seen from the τ_{xy} map where shear stresses of the order of 150 MPa can be seen along the flank face near the tool tip. This contact between the flank face and the machined surface is a result of elastic recovery of the material behind the tool tip; such elastic recovery effects have been reported in the literature, especially during machining with tools with a negative rake angle [51].

A check was made on the accuracy of the stress data by comparing the data with the reaction forces measured using the piezoelectric dynamometer. For this, the normal and shear tractions along the tool rake and flank faces were integrated and resolved along the horizontal and vertical directions to estimate F_C and F_T . This resulted in an estimate of 254 N for F_C and 217 N for F_T , whereas the respective forces measured using the dynamometer (averaged over a cutting length of

30 mm) were 262 N and 228 N. Although the exact uncertainty in the stress data is difficult to ascertain, these observations show that the overall forces estimated using photoelasticity compare well (within 5%) with the measured forces.

The nature of stress distribution along the tool rake and flank faces can be understood from Fig. 13, where the normal and shear stress profiles along these faces are plotted. As seen from Fig. 13(a), the normal stress (σ_R) on the tool rake face is maximum at the tool tip and continuously decreases with increasing distance from the tip until it drops to zero at the edge of the contact (located at about 400 μ m from the tip). The maximum normal stress at the tip was about 3 times the average pressure along the contact. Shear stress (τ_R) on the other hand shows an interesting behavior; it initially increases as one moves away from the tool tip, exhibits a maximum value of 294 MPa at about 100 μ m distance from the tip before it decreases in proportion to the normal along the rest of the contact zone. To verify whether the maximum shear stress is determined by plastic yielding of the chip along the sliding contact, an estimate was made of the chip's shear yield strength using the shear plane model [52] used in the machining literature. In this model, the material's shear flow stress (k) is estimated by treating the deformation in the primary shear zone (region OA in Fig. 2) as one of simple shear along a thin shear plane. If ϕ is the shear plane angle with respect to the V_0 direction, k can be given by:

$$k = \frac{F_S}{A_S} = \frac{(F_C \cos \phi - F_T \sin \phi) \sin \phi}{wt_0},\tag{10}$$

where F_S is the resolved shear force acting parallel to the shear plane, A_S is the shear plane area, w and t_0 are the cutting width and depth respectively, and F_C and F_T as before are the cutting and thrust forces. Using this method, k was estimated at 322 MPa which correlates well with the maximum shear stress at the contact. This observation is consistent with the general picture of sliding contacts where it is assumed that the shear stress increases with the normal stress until reaching a limit that is determined by the material's shear strength. However, the shear stress drop close to the tool tip cannot be at present reconciled with the conventional laws of sliding. As can be also inferred from the stress profiles, the friction coefficient μ (= τ_{xy}/σ_{yy}) along the tool-chip contact is hardly a constant. It increases from 0.3 near the tool tip to a value slightly greater than

1 at about 150 μ m distance from the tip, after which it remains nearly constant. It is reasonable to suppose that the contact region away from the tip, 150 μ m $< x < 400 \mu$ m, where μ is constant (shear stress proportional to normal stress), is elastic while the region near the tip ($x < 150 \mu$ m) is in a plastic state.

It should be noted that the drop in shear stress near the tool tip has been previously suggested based on conventional photoelasticity analysis of the tool-chip contact [25, 29]. However, in comparison with the previous results in the literature, the main advantage of our technique is the improved resolution, which helps clearly resolve steep stress gradients at the tool tip not only along the rake face but also along the flank face. Figure 13(b) presents the normal and shear stress profiles along the tool flank face. It can be seen that the size of this contact is small ($\sim 100 \ \mu m$ in length) and both the normal and shear stresses continuously decrease with increasing distance from the tool tip. Moreover, the fact that shear stress is less than k along the entire contact zone suggests the elastic nature of the tool flank face-machined surface contact. It is pertinent to note that in conventional analysis of machining with a sharp tool, tractions at the flank face are ignored and parameters associated with the tool rake face and chip contact, such as normal and friction forces and the coefficient of friction (μ) , are estimated by resolving the measured F_C and F_T force components along the tool rake face. Such type of calculations show that the estimated normal and tangential forces at the tool-chip contact differ substantially (by as much as 50% in the case of tangential force) from those determined using the measured stress distribution along the contact. This underscores the importance of high-resolution techniques for analyzing complex localized contacts such as in machining.

Another important application of our technique pertains to the estimation of relative contributions of the tool-chip and tool-machined surface contacts to the overall work. For this, we rely on the PIV observations (Sec. 3) which show that the velocity field at the tool-chip contact can be approximated to the first order by the bulk chip velocity V_c , which can be given by V_0t_0/t_c where t_c is the chip thickness. The work (per unit time) associated with frictional sliding at the tool-chip contact can then be obtained from $wV_c \int_L \tau_R dS$, where dS represents a line element of the tool-chip contact length denoted by L. Similarly, the frictional work at the tool flank face

and machined surface contact can be estimated using the shear stress (τ_F) data along this contact and workpiece velocity (V_0) as: $wV_0 \int_{L'} \tau_F dS$, where dS now represents a line element along the flank face-machined surface contact length (L'). These calculations show that the tool-chip contact friction contributes to 22% of the total work expended in forming the chip (given by F_CV_0), while rubbing at the flank face contributes to 14%. Thus, friction accounts for more than $1/3^{\rm rd}$ of the total work.

5.2. Wedge indentation

Similar photoelasticity measurements were carried out for wedge indentation; this section presents results obtained for a 60° (included angle) wedge plastically indenting a brass work-piece normal to its surface. Figure 14(a) shows the bright-field circular polariscope images taken at different depths (t_0) during an indentation experiment. As can be seen from the images, photoelastic fringes observed within the indenter at different t_0 are identical except for the size. For instance, it is seen that regardless of the indentation depth, the fringe order remains the same for the bulk of the indenter-workpiece contact and increases towards the contact edge near the free surface. The minimum fringe order is always observed at the central location of the indenter that is indented into the workpiece. This suggests that stress distribution within the indenter and along the indenter-workpiece contact remains identical during indentation and scales with t_0 in a geometrically similar manner. Figure 14(b) also shows that the load vs. depth curve is linear, as one would expect for a geometrically similar wedge indentation process.

In view of the geometrical similarity, photoelastic analysis of the contact stresses was made by stopping the indentation test at a specific t_0 (0.75 mm) and acquiring images required for the phase-shifting technique, see Figs. 15 and 16. After stopping the test and while acquiring images, care was taken to maintain a constant load to avoid any stress relaxation/elastic recovery effects and ensure that the data obtained is representative of the actual indentation process. As seen from Fig. 16, the fringe pattern in an interrupted indentation experiment is identical to that observed during the indentation process (see image corresponding to $t_0 = 0.75$ mm in Fig. 14). This implies that the data from an interrupted test can be used to represent stress conditions during the actual indentation process, provided that the load is maintained constant after stopping the test.

Similar to the cutting experiments, the images were post-processed and unwrapped to obtain full-field information of the principal stress directions and the fringe order, which are shown in Fig. 17. Note that a reversal in the wrapped isochromatic phase map (Fig. 17(b)) is observed along the axis of symmetry without the presence of any neutral axis. This situation is somewhat similar to the classical problem of a circular disk under uniaxial compression and can be understood by looking at some key locations on the fringe contour. For illustration purposes, the bright-field image in Fig. 16 shows five points (A-E) on the indenter face. Point A is the indenter tip, point B is the center of the indenter portion within the workpiece, C is a point located on the symmetry axis above the workpiece, D is the end of indenter-workpiece contact and E is a point above C, while the white arrows show the directions of increasing fringe order. It can be seen that point B has the minimum fringe order and acts as a sink (has a lower fringe order compared to neighborhood), whereas point C acts as a saddle point (bounded by two families of isochromatic fringes, one higher and one lower than the fringe order at C) and point D acts as a source with the largest fringe order. Thus, the fringe order is minimum at B (sink) and increases towards both A and C, which is seen as black to white transitions in the wrapped isochromatic phase map in Fig. 17(b). Considering C is the saddle point, the fringe order decreases from C to E (white to black transition), while it increases along the C to D direction (black to white transition).

The isoclinic and isochromatic data were then used with the shear difference technique to obtain full-field stress data over the indenter. A check on the accuracy of the stress data was made by comparing it with the load cell data, which showed that the vertical force component estimated using photoelasticity was within 6% of the measured force value. Note that photoelasticity also allows us to estimate the horizontal force component, which cannot be measured directly since the opposite horizontal force components get balanced out in indentation.

Figure 18 shows the stress maps for four components: σ_{xx} , σ_{yy} , τ_{xy} and σ_h . The stress state at the indenter tip is seen to be highly compressive and remains uniform over the bulk of the contact length. For example, see Fig. 19 (a) which shows the variation of normal stress (σ_{yy}) and shear stress (τ_{xy}) along the contact. Unlike cutting where normal stress shows a steep gradient near the tool tip, a nearly constant contact pressure (normal stress) is observed over the bulk of the

contact, followed by a gradual decay towards the contact edge near the free surface ($x \sim 800 \ \mu \text{m}$). It appears that the workpiece in contact with the indenter over the zone of constant pressure is in a plastic state while the zone near the contact edge is likely supported by elastic stresses within the workpiece (also see discussion in Sec. 6).

A closer inspection of the shear stress field in Fig. 18(c) shows that there exists a small zone near the indenter tip where the shear stress is non-negligible. In fact, as seen from Fig. 19 (a), shear stress along the contact is close to k at the indenter tip and further decreases with increasing distance from the tip, dropping to zero about midway of the contact length. Similarly, the friction coefficient μ decreases continuously along the contact from a value of 0.2 at the tip to zero at $x \sim 400~\mu\text{m}$. This observation is in direct contrast to that in cutting where μ increases from the tool tip to the contact edge; a physical explanation for this observation is lacking at the present time. Previously, it has been postulated that friction effects may be important in indentation with sharp indenters (small included angles) where there is gross slip at the indenter and specimen contact. However, the difficulty of measuring the horizontal force component in indentation, which is required to compute the tangential force along the indenter face, has precluded any experimental analysis of friction. The photoelasticity measurements presented here overcome this problem and allows direct examination of frictional effects in indentation. An estimate of the frictional work at the indenter-workpiece contact, made using the shear stress distribution and slip velocity at this interface, shows that it contributes to 6% of the overall indentation work.

Before concluding this section, it is pertinent to briefly discuss the effect of specimen width (w) on the plane-strain condition since the stress data was obtained based on this assumption. In the literature, a width to depth ratio of 5 or above is generally considered necessary before one can neglect out-of-plane material spread near the specimen edges and treat the problem as plane-strain [53]. In our cutting experiments, the w/t_0 ratio is ~ 50 therefore, plane-strain conditions must prevail across the bulk of the specimen width. On the other hand, the indentation depth at which the measurements were made (Figs. 15-19) corresponds to a w/t_0 ratio of 4. To understand the effect of the w/t_0 ratio, indentation experiments were carried out with different w/t_0 ratios, and results from these experiments are included as Appendix. The main finding from these experiments

was that although a w/t_0 ratio > 8 is needed to ensure plane-strain conditions, the out-of-plane spread at the specimen edges observed with smaller ratios did not have a significant effect on the stress data, see Fig. A3 in the Appendix for more details.

6. Discussion

Digital photoelasticity coupled with sapphire as a cutting tool/indenter has allowed direct measurement of stresses over the sliding plastic contact in sharp wedge indentation and machining of metals. While digital imaging and phase-shifting technique enables full-field measurements of stresses at high resolution, thus providing the ability to resolve steep stress gradients intrinsic to indentation and machining contacts, the use of sapphire (instead of soft photoelastic model materials) as a tool material makes it possible to obtain data with any metal. Measurements of contact stress distributions made in the paper for indentation and cutting experiments with a ductile metal (70/30 brass) have helped characterize and reveal several important features of the contact including the elastic-plastic transition, variation of friction coefficient along the contact, and the limits imposed on contact stresses by metal plasticity. When coupled with complementary observations of material sliding at the tool-workpiece interface, digital photoelasticity proves to be a promising tool for quantifying frictional dissipation in sliding contacts.

Elastic-plastic transition along the contact for instance can be understood from the normal stress distribution in wedge indentation. As seen from Fig. 19(a), normal stress (pressure) is uniform over nearly 2/3rds of the contact length and shows a gradual decay near the edge. The problem of plane-strain wedge indentation of a rigid-perfectly plastic material was studied by Hill [40] using slip-line field theory, and this analysis predicts a uniform pressure distribution along the entire indenter face. The solution to the other extreme case, that of wedge indentation of a perfectly elastic material, due to Sneddon [54], on the other hand, predicts zero pressure at the end of the contact and that pressure should increase rapidly as one moves closer to the indenter tip, becoming infinite at the tip. Considering these, our observations suggest that the material points in contact with the indenter near the edge are elastically loaded, whereas points away from the edge, upon reaching the limit pressure (solid black horizontal line, Fig. 19(b)), are plastically

deformed and sustain a constant pressure. A quantitative comparison of the data with the elastic solution is shown in Fig. 19(b). The elastic solution for pressure distribution along the contact in wedge indentation is given by:

$$p = \frac{\delta}{\pi a} \frac{E_1}{1 - \nu_1^2} \cosh^{-1} \left(\frac{1}{x}\right),\tag{11}$$

where x is the distance from the indenter tip normalized with the contact length (i.e., x = 0 and x = 1 correspond to the indenter tip and contact edge, respectively), a is the indentation width, E_1 and ν_1 are the elastic modulus and Poisson's ratio of the workpiece, and δ is the indentation depth. However, instead of using the *total* indentation depth, only the *elastic* (recoverable) portion of the indentation depth was used in the above equation. Following Stillwell and Tabor's analysis [55] and adapting it for the case of wedge, δ can be given by:

$$\delta = \frac{2P}{\pi w} (1 + \log 2) \left(\frac{1 - \nu_1^2}{E_1} + \frac{1 - \nu_2^2}{E_2} \right), \tag{12}$$

where P is the indentation load, and E_2 and ν_2 are the material properties of the indenter. The curve predicted by the above elastic solution is shown as a dashed black curve in Fig. 19(b). As can be seen, the elastic solution captures the pressure variation near the contact edge reasonably well, suggesting that this region is likely supported by an elastic stress field within the workpiece. It is also interesting to note that the elastic contact zone near the edge is not negligible but makes up about $1/3^{\rm rd}$ of the contact length, which is somewhat surprising given the high E/σ_f ratio of brass, since large E/σ_f ratios are generally considered to be representative of rigid plastic materials where elastic effects are of secondary importance. In this context, reference should be made to Johnson [56] who suggested that whether the elastic or plastic effects dominate in indentation can be assessed using a single parameter $(E/\sigma_f) \tan \beta$, where β is the angle between the indenter face and specimen surface. Johnson postulated that as this parameter increases in value, the contact state transitions from a purely elastic to elastic-plastic and then to a fully plastic state for

parameter values greater than 100. For reference, $(E/\sigma_f) \tan \beta \approx 450$ in our case. This discrepancy is perhaps due to the fact that Johnson's analysis is based on the expanding cavity theory which does not directly apply to the cutting deformation mode observed in indentation with sharp wedges $(\beta > 30^{\circ})$. Regardless, the experimental capability to obtain contact stress distribution provides an interesting tool to assess the relative significance of elastic and plastic effects in indentation as a function of material properties (E, σ_f) and indenter geometry (β) .

Another important observation that emerges from our study relates to the upper limit on the contact shear stress imposed by the material's shear flow stress (k). This was observed in both indentation and cutting (although the location of maximum shear stress is different in both cases) and is consistent with our general understanding of sliding contacts that when τ reaches k, further increase in stress is limited by local plastic flow at the contact. Equally importantly, the study also highlights certain features of the sliding contact that cannot be fully reconciled with the conventional friction models. Taking indentation as an example (Fig. 19), the shear stress variation is such that it decreases from a value close to k at the indenter tip to zero at about midway of the contact length despite the pressure (normal stress) being uniform over this region. This results in continuous variation of friction coefficient along the contact that cannot be explained using the Coulomb's model or the capped Coulomb's model.

The situation is even more complex in cutting where shear stress exhibits a non-monotonic behavior with a peak located at a distance from the tool tip, while normal stress shows a continuous decrease with increasing distance from the tip. Clues about the origin of this complex stress distribution can be perhaps derived by correlating stresses with the local material flow at the tool-chip contact. For example, Ackroyd et al. [57] presented a comprehensive model for the contact conditions at the tool-chip interface based on direct observations of chip flow at the contact using a transparent cutting tool. Based on experimental observations, Ackroyd et al. represented the tool-chip contact by categorizing it into four regions: (I) a region of stagnation at the tool tip, (II) a region of retardation adjacent to the stagnation region, (III) a sliding region, followed by (IV) a sticking region where material from the chip underside transferred onto the tool rake face in the form of deposits. They also noted that the stagnation region is more prominent in the case

of cutting tools with a negative rake angle. Now considering the shear stress distribution along the rake face shown in Fig. 13(a), we see that it can be likewise categorized into four regions: a region of small shear stress at the cutting edge, a region of constant shear stress in the middle, followed by a region where the shear stress decreases in proportion to the normal stress, and finally a region of almost zero shear stress at the edge of the contact. This representation correlates well with the model presented by Ackroyd et al. [57] and provides a basis for small shear stress in region I (due to material stagnation), constant shear stress ($\tau \sim k$) in region II where the chip underside is plastically deformed and its flow retarded as it slides against the tool face, and the constant μ in region III in accordance with Coulomb's law where material slides with the same velocity as that of the bulk of the chip. We also note that in similar experiments performed with tools with a positive rake angle, no dip in the shear stress was observed at the cutting edge; in this case, the shear stress remains constant at $\sim k$ for some distance along the tool-chip interface and monotonically decreases towards the contact edge. This is consistent with the absence of stagnation region I when machining with tools having a positive rake angle [57].

Taken together, the observations reported in the paper underscore the complex nature of sliding plastic contacts – their deviation from the conventional laws of sliding friction as well as their high sensitivity to the contact geometry. In view of the close relationship between the stress state and material flow conditions at the contact, it would be of interest to perform stress measurements and observe the contact, simultaneously. In this regard, the use of sapphire provides a unique opportunity as it can be not only used for photoelastic measurements but is also transparent. For example, a modification to the standard tool geometry to include an inclined facet that allows one to view internally reflected image of the tool-chip contact from the side of the tool can be utilized for this purpose; such direct experimental observations of the contact zone in machining were pioneered by Nakayama [58] and also later made by others [59, 60].

Such experiments would be also valuable from a modeling perspective. For example, in the machining literature, various friction models have been proposed for the tool-chip sliding contact, with Zorev's sticking-sliding contact zone model [61] being the most commonly used model. In this model, the normal stress over the rake face is described to vary as a power law with the distance

from the cutting edge, rising from a value of zero at the chip separation point to a maximum value at the cutting edge. Shear stress on the other hand is modeled using two separate zones: (1) "sticking" zone near the cutting edge characterized by a constant shear stress (assumed to be equal to k for dry machining), and (ii) "sliding" zone where shear stress is taken to vary proportional to the normal stress with a constant coefficient of friction (Coulomb's law). This is the most commonly used friction law in finite element simulations of machining [62], although note that this characterization of the tool-chip contact into sticking and sliding zones is in contrast to the actual experimental observations in Ref. [57]. A similar friction law that captures the transition between constant shear stress near the cutting edge to Coulomb friction near the trailing edge of the tool-chip contact has been also proposed by Shirakashi and Usui [63]. The contact stress measurements such as those presented in this paper can be used to evaluate different friction models and map out machining conditions where these models provide a reasonable approximation of the actual boundary conditions.

Another potential application pertains to understanding the action of cutting fluids. That the use of cutting fluids can lead to substantial reductions in the friction force, especially under low machining speeds, is well-known [64]. The photoelasticity technique can be used to directly characterize the effect of cutting fluid lubrication on tool-chip contact stress distribution and resulting forces, and how fluid properties such as viscosity and fluid film thickness affect the stress profiles. While our study has specifically focused on indentation and cutting, with suitable design modifications, the experimental method can be applied to study a wide range of sliding plastic contact problems of relevance to materials processes and understand the parameter effects (sliding speed, lubrication, etc.) therein on contact stresses. Recent developments in high-speed imaging and dynamic photoelasticity, such as using a camera sensor with a pixelated micro-retarder array to determine stresses from a single image [65, 66], also hold promise for studying non-steady problems and time-varying frictional conditions.

7. Concluding Remarks

A full-field experimental method for quantifying interfacial stresses and friction along sliding plastic contacts is described and implemented to study interactions between a rigid tool (indenter) and a ductile metal in two problems: plane-straining machining and wedge indentation. The method is based on digital photoelasticity combined with the use of sapphire as the photoelastic tool material. It is shown that when compared to the conventional photoelasticity technique, the method is significantly superior in terms of the ability to map stresses at high spatial resolution (~ 1 μ m per pixel) and resolve steep stress gradients near the tip of the tool. The method has allowed detailed measurements of stress distribution (both normal and tangential stress components) at and near the tool-metal interface and helped characterize other key features of the contact such as elastic-plastic boundary, variation of sliding friction coefficient along the contact, and friction contribution to the overall work. An attempt has been made to link the observed contact stress profiles with the kinematics of metal plastic flow at the interface, and a good correlation was found. The high-resolution contact stress measurements reported in the paper constitute an important step towards developing a unified friction law for sliding plastic contacts and further understanding of the effect of contact geometry and lubrication in materials processes. The method should also be valuable for quantifying and incorporating the effect of friction in indentation tests used to characterize the mechanical properties of materials.

Acknowledgments

Funding support by the US National Science Foundation through grant no. CMMI- 2102030 is gratefully acknowledged. The authors would also like to thank Randy Carlson of the Houston Gem and Mineral Society for discussions and help with preparation of the sapphire tools.

Appendix A. Analysis of sources of error in photoelasticity measurements

In our analysis of contact stresses in wedge indentation, there were three main assumptions:

- 1. The indentation process is geometrically similar, that is, the stress distribution is identical in magnitude and shape at all depths of indentation (t_0) ;
- 2. The stress distribution during indentation and that is measured in an interrupted test (with the load maintained constant) are the same; and
- 3. Plane-strain assumption, meaning that all planes along the width direction have the same stress distribution.

The first assumption has been verified by the identical nature of fringe contours at different t_0 (see Fig. 14), while the similarity in the bright-field isochromatic images captured during indentation and in an interrupted test (cf. Fig. 16(a) and image in Fig. 14 at $t_0 = 0.75$ mm) validates the second assumption. We now proceed with verifying the third assumption. To investigate the effect of the w/t_0 ratio on the plane-strain assumption, we performed indentation experiments with three w/t_0 ratios: 4, 9, and 15. This was achieved by varying the indenter/specimen width and maintaining t_0 in the 0.6-0.75 mm range. Figure A1 shows the top view of the indentation tracks achieved under w/t_0 ratios. Note that in these images, the horizontal dimension is the specimen width and the indentation loading axis is into the plane of the image. It can be seen that when w/t_0 is small (Fig. A1(a)), the specimen shows considerable lateral flow along the width direction at its edges. However, the extent of this lateral flow is greatly diminished at larger w/t_0 ratios (Figs. A1(b) and (c)), and under such conditions, the two-dimensional plane-strain assumption should be valid.

Photoelastic stress measurements have been also made to investigate any potential differences in indentation stress fields among the experiments carried out with different w/t_0 ratios. As discussed in Sec. 4, a color camera together with a white LED was originally utilized for photoelastic measurements. The use of color camera was intended to eliminate the isoclinic-isochromatic interaction in the plane polariscope arrangements, and thus obtain error-free principal stress directions. Also, only the red channel in the six images captured in the circular polariscope arrangement was used for the fringe order estimation. However, at large specimen widths that were used to achieve

higher w/t_0 ratios, an extremely high density of isochromatic fringes was observed due to more number of planes contributing to the retardation imparted on the incident light. This high fringe density resulted in low contrast and smudging of the fringes, which made the data not suitable for post-processing. To overcome this issue, the image acquisition module of the experimental setup was modified to accommodate two cameras (one color and one monochromatic) simultaneously, with a non-polarizing cube beam splitter placed in between the cameras and the lens, see Fig. A2. The non-polarizing beam splitter splits the incident light into two with a reflection/transmission ratio of 50/50, maintaining the incident light's original polarization state. This modification allowed for simultaneous capture of both the color and monochromatic images. For the ten-step PST, plane polariscope images were captured using a color camera and white LED as the light source, while for the circular polariscope arrangement, the images were captured using a monochromatic camera and red LED as the light source. The monochromatic camera along with a monochromatic light source provided images with substantially improved contrast at regions with a high density of isochromatic fringes. The unwrapped isoclinic and isochromatic parameters were obtained using the quality guided phase unwrapping algorithm. As before, the shear difference technique was then used to obtain the individual stress components.

Figure A3(a) shows the normal and shear stress distribution at the indenter/workpiece contact for all three cases. In Fig. A3(b), the data is replotted after normalizing the x-axis (distance from the tool tip) with the respective contact length for each case. It can be seen that all the normalized plots fall on the same curve. This suggests the secondary nature of lateral material flow effects on the obtained stress data even under small w/t_0 ratios.

References

- [1] M. C. Shaw, The role of friction in deformation processing, Wear 6 (2) (1963) 140–158.
- [2] J. A. Schey, Tribology in Metalworking: Friction, Lubrication and Wear, American Society for Metals, Metals Park, OH, 1983.
- [3] F. P. Bowden, D. Tabor, The Friction and Lubrication of Solids: Part II, Oxford University Press, London, UK, 1964
- [4] A. G. Atkins, D. Tabor, Plastic indentation in metals with cones, Journal of the Mechanics and Physics of Solids 13 (3) (1965) 149–164.
- [5] A. DiCarlo, H. T. Y. Yang, S. Chandrasekar, Prediction of stress-strain relation using cone indentation: Effect of friction, International Journal for Numerical Methods in Engineering 60 (3) (2004) 661–674.
- [6] A. K. Bhattacharya, W. D. Nix, Finite element simulation of indentation experiments, International Journal of Solids and Structures 24 (9) (1988) 881–891.
- [7] M. Mata, J. Alcala, The role of friction on sharp indentation, Journal of the Mechanics and Physics of Solids 52 (1) (2004) 145–165.
- [8] H. Chandrasekaran, R. Nagarajan, K. N. Padmanabhan, Application of moiré technique in the stress analysis of cutting tools, Strain 14 (2) (1978) 64–71.
- [9] P. S. Theocaris, C. A. Stassinakis, The determination of coefficient of friction between a cylindrical indenter and a plastically deformed body by caustics, International Journal of Mechanical Sciences 24 (12) (1982) 717–727.
- [10] P. S. Theocaris, C. A. Stassinakis, A. G. Mamalis, Roll-pressure distribution and coefficient of friction in hot rolling by caustics, International Journal of Mechanical Sciences 25 (11) (1983) 833–844.
- [11] S. Kato, K. Yamaguchi, M. Yamada, Stress distribution at the interface between tool and chip in machining, Journal of Engineering for Industry 94 (1972) 683–689.
- [12] G. Barrow, W. Graham, T. Kurimoto, Y. F. Leong, Determination of rake face stress distribution in orthogonal machining, International Journal of Machine Tool Design and Research 22 (1) (1982) 75–85.
- [13] T. H. C. Childs, M. I. Mahdi, G. Barrow, On the stress distribution between the chip and tool during metal turning, CIRP Annals 38 (1) (1989) 55–58.
- [14] D. Buryta, R. Sowerby, I. Yellowley, Stress distributions on the rake face during orthogonal machining, International Journal of Machine Tools and Manufacture 34 (5) (1994) 721–739.
- [15] M. M. Frocht, Photoelasticity, John Wiley and Sons, Inc., New York, 1941.
- [16] H. Aben, C. Guillemet, Photoelasticity of Glass, Springer Science & Business Media, 1993.
- [17] P. M. Cook, J. G. Wistreich, Measurement of die pressures in wire drawing by photoelastic methods, British Journal of Applied Physics 3 (5) (1952) 159.
- [18] Y. Ohashi, S. Murakami, K. Nishikiori, A photoelastic analysis for the stress distribution in roller-dies for strip drawing, International Journal of Mechanical Sciences 6 (6) (1964) 461–471.

- [19] Y. Ohashi, K. Nishikiori, Photoelastic investigation of plane wedge-shaped drawing die, Experimental Mechanics 6 (1966) 171–176.
- [20] F. A. Khayyat, P. R. Lancaster, A photoelastic examination of the stresses in rolls during rolling, Journal of Strain Analysis 4 (4) (1969) 245–260.
- [21] M. I. Ghobrial, A photoelastic investigation on the contact stresses developed in rolls during asymmetrical flat rolling, International Journal of Mechanical Sciences 31 (10) (1989) 751–764.
- [22] E. P. Unksov, Y. S. Safarov, A photoelastic investigation of contact stresses in the backward extrusion process, International Journal of Mechanical Sciences 17 (10) (1975) 597–602.
- [23] M. Okoshi, S. Fukui, Studies of cutting action by means of photoelasticity, Journal of the Society of Precision Mechanics of Japan 1 (1934) 598.
- [24] E. Usui, H. Takeyama, A photoelastic analysis of machining stresses, Journal of Engineering for Industry 84 (1960) 303–307.
- [25] H. Chandrasekaran, D. V. Kapoor, Photoelastic analysis of tool-chip interface stresses, Journal of Engineering for Industry 87 (1965) 495–502.
- [26] E. Amini, Photoelastic analysis of stresses and forces in steady cutting, Journal of Strain Analysis 3 (3) (1968) 206–213.
- [27] S. Ramalingam, A photoelastic study of stress distribution during orthogonal cutting Part 2: Photoplasticity observations, Journal of Engineering for Industry 93 (1971) 538–544.
- [28] E. G. Coker, N. F. Filon, Treatise on Photoelasticity, Cambridge University Press, 1957.
- [29] A. Bagchi, P. K. Wright, Stress analysis in machining with the use of sapphire tools, Proceedings of the Royal Society of London. A. Mathematical and Physical Sciences 409 (1836) (1987) 99–113.
- [30] S. D. K. Barbat, R. S. Rao, Photoelastic investigation of metal-forming processes using new sapphire dies, Experimental Techniques (1990) 40–43.
- [31] S. Yoshida, S. Iwata, T. Sugawara, Y. Miura, J. Matsuoka, A. Errapart, C. R. Kurkjian, Elastic and residual stresses around ball indentations on glasses using a micro-photoelastic technique, Journal of Non-Crystalline Solids 358 (24) (2012) 3465–3472.
- [32] Y. Yokoyama, B. R. Mitchell, A. Nassiri, B. L. Kinsey, Y. P. Korkolis, Y. Tagawa, Integrated photoelasticity in a soft material: Phase retardation, azimuthal angle, and stress-optic coefficient, Optics and Lasers in Engineering 161 (2023) 107335.
- [33] B. Mitchell, Y. Yokoyama, A. Nassiri, Y. Tagawa, Y. P. Korkolis, B. L. Kinsey, An investigation of Hertzian contact in soft materials using photoelastic tomography, Journal of the Mechanics and Physics of Solids 171 (2023) 105164.
- [34] R. J. Adrian, J. Westerweel, Particle Image Velocimetry, Cambridge University Press, 2011.
- [35] S. Yadav, D. Sagapuram, In situ analysis of shear bands and boundary layer formation in metals, Proceedings of the Royal Society A 476 (2234) (2020) 20190519.

- [36] H. Chawla, S. Yadav, H. Aprahamian, D. Sagapuram, Determining large-strain metal plasticity parameters using in situ measurements of plastic flow past a wedge, Proceedings of the Royal Society A 479 (2275) (2023) 20230061.
- [37] D. Sagapuram, A. Udupa, K. Viswanathan, J. B. Mann, R. M'Saoubi, T. Sugihara, S. Chandrasekar, On the cutting of metals: A mechanics viewpoint, Journal of Manufacturing Science and Engineering 142 (11) (2020) 110808.
- [38] P. K. Wright, J. G. Horne, D. Tabor, Boundary conditions at the chip-tool interface in machining: Comparisons between seizure and sliding friction, Wear 54 (2) (1979) 371–390.
- [39] K. L. Johnson, Contact Mechanics, Cambridge University Press, Cambridge, UK, 1985.
- [40] R. Hill, The Mathematical Theory of Plasticity, Clarendon Press, Oxford, UK, 1950.
- [41] L. E. Samuels, T. O. Mulhearn, An experimental investigation of the deformed zone associated with indentation hardness impressions, Journal of the Mechanics and Physics of Solids 5 (2) (1957) 125–134.
- [42] N. K. Sundaram, Mechanics of plastic flow past a narrow-angle wedge indenter, Philosophical Magazine 99 (23) (2019) 2883–2903.
- [43] S. Timoshenko, J. N. Goodier, Theory of Elasticity, McGraw-Hill Book Company, New York, 1951.
- [44] K. Ramesh, S. Sasikumar, Digital photoelasticity: Recent developments and diverse applications, Optics and Lasers in Engineering 135 (2020) 106186.
- [45] M. Ramji, K. Ramesh, Whole field evaluation of stress components in digital photoelasticity—Issues, implementation and application, Optics and Lasers in Engineering 46 (3) (2008) 257–271.
- [46] T. M. Jobin, S. N. Khaderi, M. Ramji, Experimental evaluation of the strain intensity factor at the inclusion tip using digital photoelasticity, Optics and Lasers in Engineering 126 (2020) 105855.
- [47] M. Ramji, K. Ramesh, Adaptive quality guided phase unwrapping algorithm for whole-field digital photoelastic parameter estimation of complex models, Strain 46 (2) (2010) 184–194.
- [48] R. V. Mahajan, K. Ravi-Chandar, Experimental determination of stress-intensity factors using caustics and photoelasticity, Experimental Mechanics 29 (1989) 6–11.
- [49] M. Solaguren-Beascoa Fernández, J. M. Alegre Calderón, P. M. Bravo Diez, I. I. Cuesta Segura, Stress-separation techniques in photoelasticity: A review, The Journal of Strain Analysis for Engineering Design 45 (1) (2010) 1–17.
- [50] F. Vadovič, Contribution to the analysis of errors in photoelasticity: Application of theory of errors to some numerical methods used in photoelasticity to separate the principal stresses yields greater accuracy, Experimental Mechanics 5 (1965) 413–416.
- [51] M. E. Abdelmoneim, R. F. Scrutton, Post-machining plastic recovery and the law of abrasive wear, Wear 24 (1) (1973) 1–13.
- [52] M. E. Merchant, Mechanics of the metal cutting process. II. Plasticity conditions in orthogonal cutting, Journal of Applied Physics 16 (6) (1945) 318–324.

- [53] W. A. Backofen, Deformation Processing, Addison-Wesley Publishing Company, 1972.
- [54] I. N. Sneddon, Fourier Transforms, Dover Publications, 1995.
- [55] N. A. Stilwell, D. Tabor, Elastic recovery of conical indentations, Proceedings of the Physical Society 78 (2) (1961) 169.
- [56] K. L. Johnson, The correlation of indentation experiments, Journal of the Mechanics and Physics of Solids 18 (2) (1970) 115–126.
- [57] B. Ackroyd, S. Chandrasekar, W. D. Compton, A model for the contact conditions at the chip-tool interface in machining, Journal of Tribology 125 (3) (2003) 649–660.
- [58] K. Nakayama, Studies on the mechanism of metal cutting, Bulletin of the Faculty of Engineering, Yokohama National University 7 (1959) 1–26.
- [59] E. D. Doyle, J. G. Horne, D. Tabor, Frictional interactions between chip and rake face in continuous chip formation, Proceedings of the Royal Society of London. A. Mathematical and Physical Sciences 366 (1725) (1979) 173–183.
- [60] V. Madhavan, S. Chandrasekar, T. N. Farris, Direct observations of the chip-tool interface in the low speed cutting of pure metals, Journal of Tribology 124 (3) (2002) 617–626.
- [61] N. N. Zorev, Metal Cutting Mechanics, Pergamon Press, Oxford, England, 1966.
- [62] S. N. Melkote, W. Grzesik, J. Outeiro, J. Rech, V. Schulze, H. Attia, P. J. Arrazola, R. M'Saoubi, C. Saldana, Advances in material and friction data for modelling of metal machining, CIRP Annals 66 (2) (2017) 731–754.
- [63] T. Shirakashi, E. Usui, Friction characteristics on tool face in metal machining, Journal of the Japanese Society of Precision Engineering 39 (9) (1973) 966–971.
- [64] J. A. Williams, The action of lubricants in metal cutting, Journal of Mechanical Engineering Science 19 (5) (1977) 202–212.
- [65] S. Yoneyama, H. Kikuta, K. Moriwaki, Simultaneous observation of phase-stepped photoelastic fringes using a pixelated microretarder array, Optical Engineering 45 (8) (2006) 083604–083604.
- [66] H. Zhang, S. Jia, B. Wen, Z. Yang, X. Zhou, Z. Lin, L. Wang, Advancing instantaneous photoelastic method with color polarization camera, Optics and Lasers in Engineering 172 (2024) 107868.

Table 1: Ten-step phase-shifting technique (PST): Optical arrangements and the respective intensity equations.

| α | ζ | η | β | Intensity Equation |
|------------------|------------------|------------------|------------------|---|
| $\frac{\pi}{2}$ | - | - | 0 | $I_1 = I_b + I_a \sin^2(\frac{\delta}{2}) \sin^2 2\theta$ |
| $\frac{5\pi}{8}$ | - | - | $\frac{\pi}{8}$ | $I_2 = I_b + \frac{I_a}{2}\sin^2(\frac{\delta}{2})(1 - \sin 4\theta)$ |
| $\frac{3\pi}{4}$ | - | - | $\frac{\pi}{4}$ | $I_3 = I_b + I_a \sin^2(\frac{\delta}{2}) \cos^2 2\theta$ |
| $\frac{7\pi}{8}$ | - | - | $\frac{3\pi}{8}$ | $I_4 = I_b + \frac{I_a}{2}\sin^2(\frac{\delta}{2})(1 + \sin 4\theta)$ |
| $\frac{\pi}{2}$ | $\frac{3\pi}{4}$ | $\frac{\pi}{4}$ | $\frac{\pi}{2}$ | $I_5 = I_b + \frac{I_a}{2}(1 + \cos \delta)$ |
| $\frac{\pi}{2}$ | $\frac{3\pi}{4}$ | $\frac{\pi}{4}$ | 0 | $I_6 = I_b + \frac{I_a}{2}(1 - \cos \delta)$ |
| $\frac{\pi}{2}$ | $\frac{3\pi}{4}$ | 0 | 0 | $I_7 = I_b + \frac{I_a}{2}(1 - \sin 2\theta \sin \delta)$ |
| $\frac{\pi}{2}$ | $\frac{3\pi}{4}$ | $\frac{\pi}{4}$ | $\frac{\pi}{4}$ | $I_8 = I_b + \frac{I_a}{2}(1 + \cos 2\theta \sin \delta)$ |
| $\frac{\pi}{2}$ | $\frac{\pi}{4}$ | 0 | 0 | $I_9 = I_b + \frac{I_a}{2}(1 + \sin 2\theta \sin \delta)$ |
| $\frac{\pi}{2}$ | $\frac{\pi}{4}$ | $\frac{3\pi}{4}$ | $\frac{\pi}{4}$ | $I_{10} = I_b + \frac{I_a}{2}(1 - \cos 2\theta \sin \delta)$ |

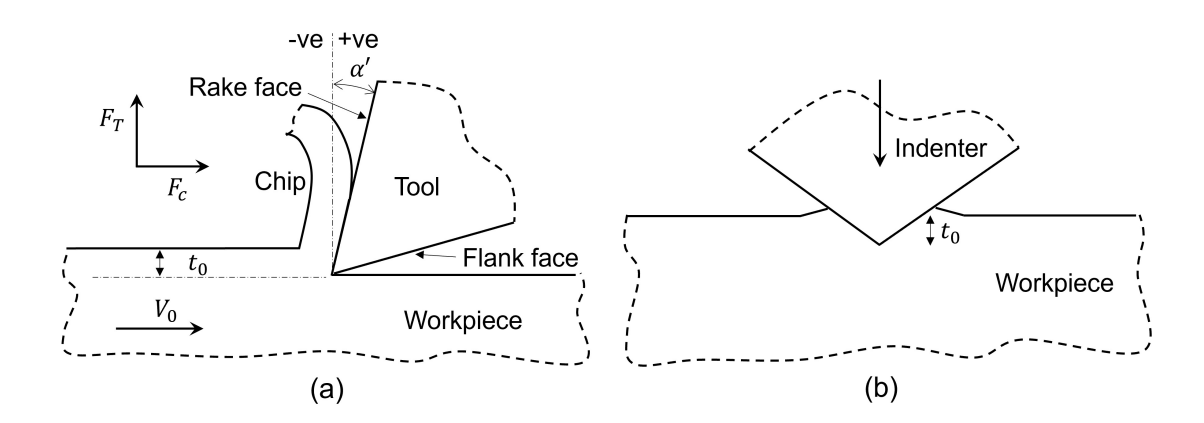


Figure 1: Schematic of plane-strain cutting (a) and (b) wedge indentation (b). V_0 : cutting speed, α' : tool rake angle, t_0 : cutting or indentation depth.

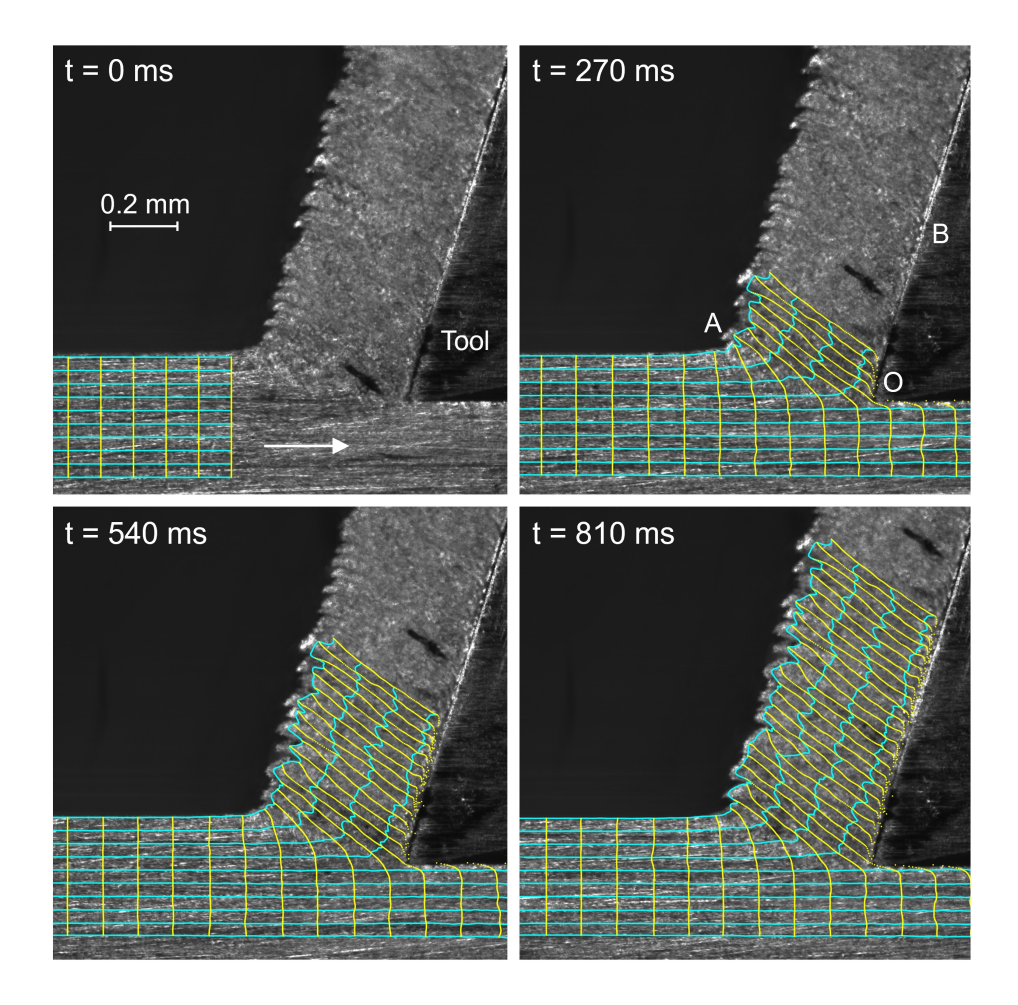


Figure 2: Images captured at different time instances during cutting of single-phase brass. The superimposed grid obtained using PIV shows plastic deformation at the primary shear zone OA and also along the tool-chip sliding contact OB. Cutting velocity $(V_0) = 4$ mm/s, cutting depth $(t_0) = 135$ μ m, imaging frame rate = 2,000 fps.

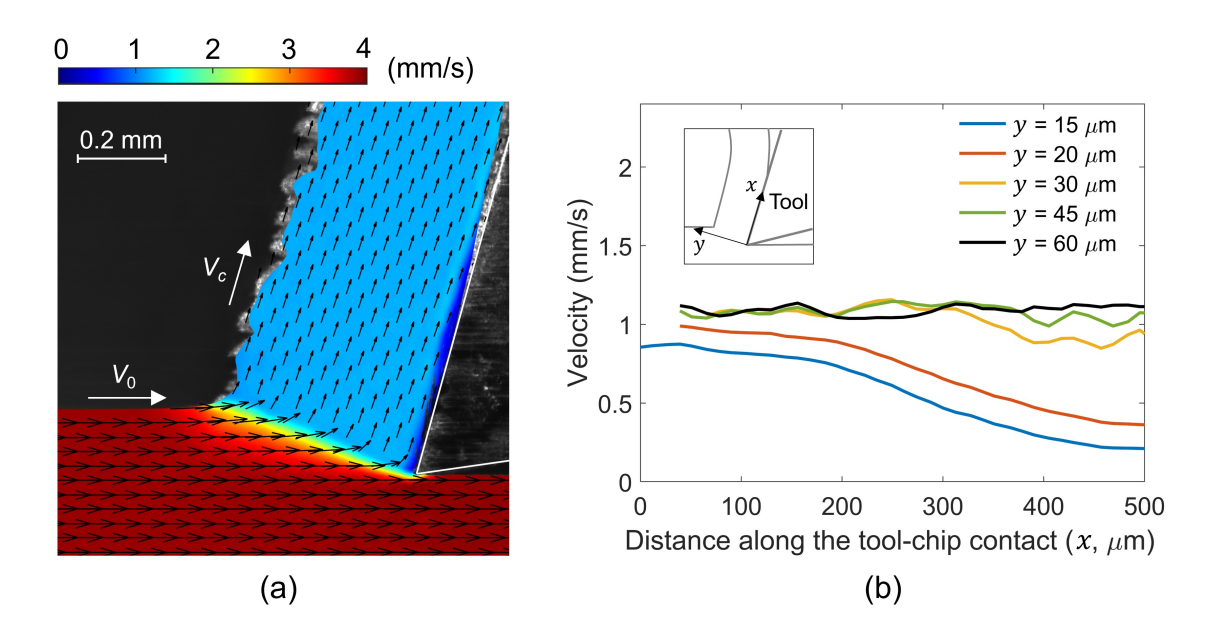


Figure 3: Velocity field in cutting: (a) velocity contour map with superimposed quiver plot, and (b) velocity distribution in the chip near the tool-chip interface plotted as a function of distance from the cutting edge (x) at different normal distances from the tool face (y). Both the figures show local velocity gradient at the tool-chip interface due to secondary plastic flow. Same cutting conditions as in Fig. 2.

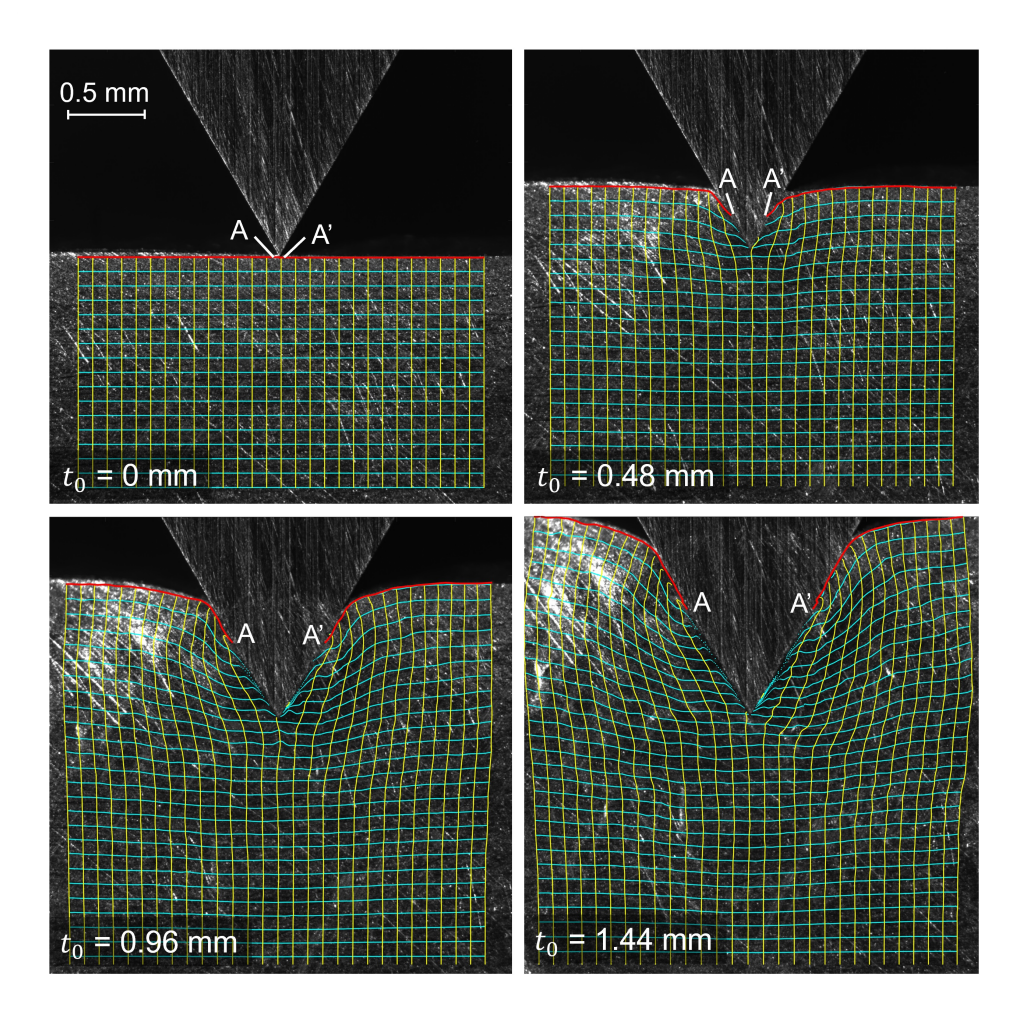


Figure 4: PIV grid showing the evolution of plastic deformation field in wedge indentation. The evolution of specimen's surface (red line) also illustrates the "cutting" deformation mode at the indenter tip, see text for additional details. Wedge angle $=60^{\circ}$, indentation speed =0.5 mm/s, imaging frame rate =500 fps.

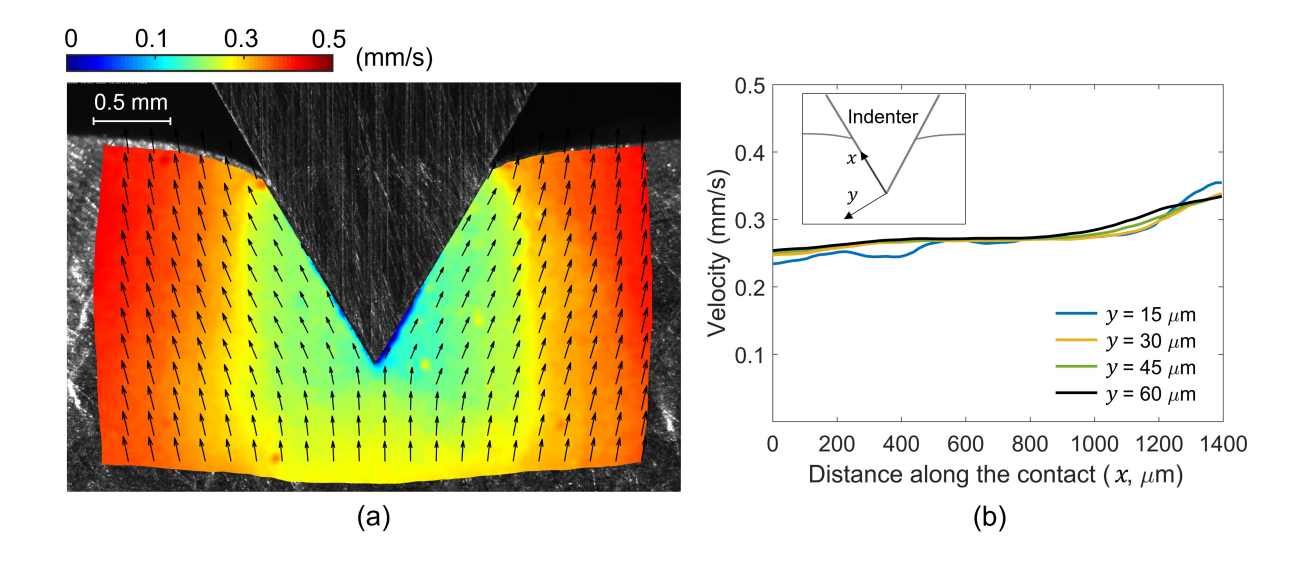


Figure 5: Velocity field in wedge indentation: (a) velocity contour map with a quiver plot, and (b) velocity distribution near the indenter-workpiece interface plotted as a function of x (distance along the interface from the indenter tip) and y (normal distance from the interface). Note the nearly uniform sliding velocity along the interface. In this experiment, the indenter was stationary and workpiece was moved vertically against the indenter at a constant velocity of 0.5 mm/s.

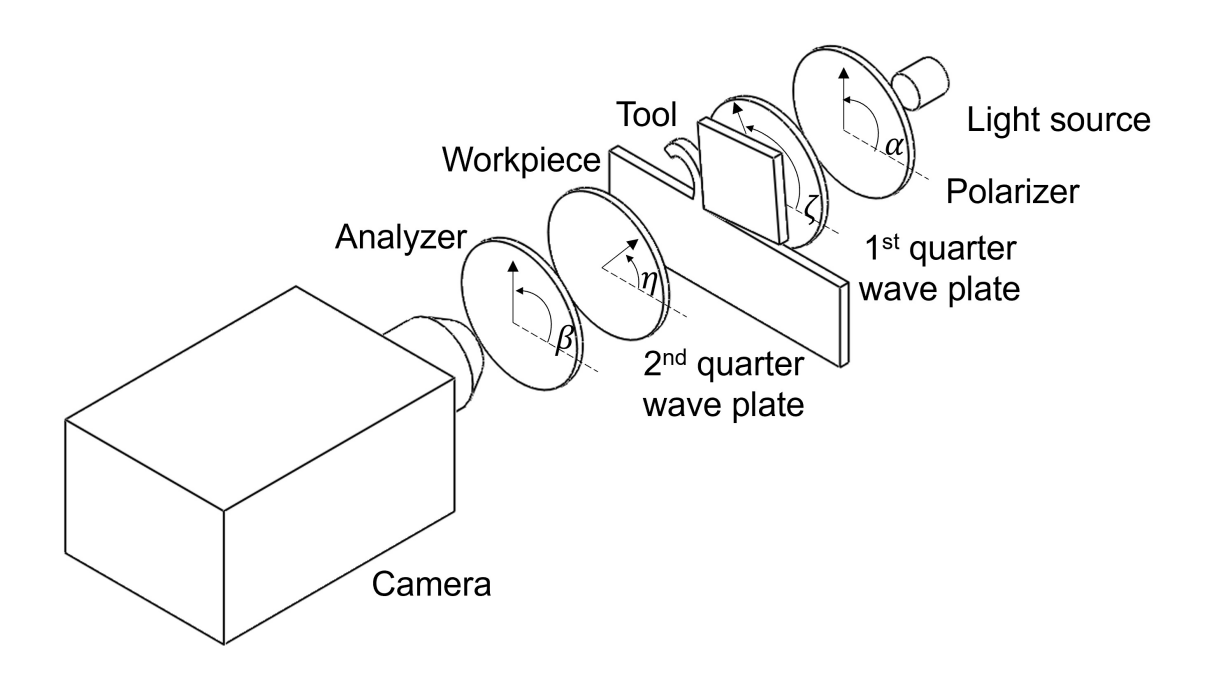


Figure 6: Schematic of the polariscope arrangement consisting of a light source, polarizer, quarter-wave plates, analyzer, camera, and the sapphire tool/indenter in between the two quarter-wave plates.

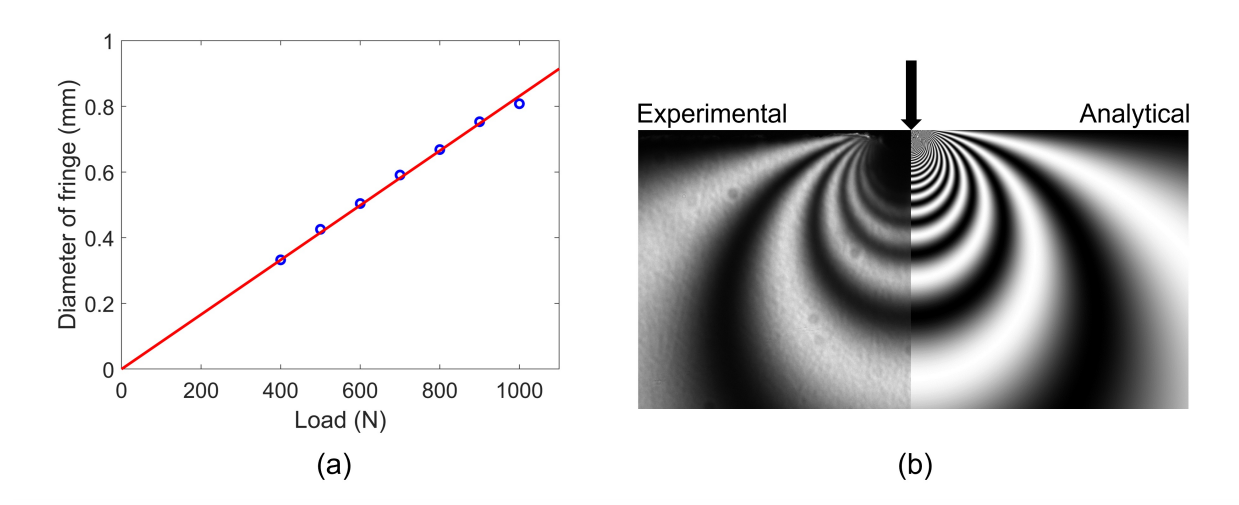


Figure 7: (a) Variation of the fringe diameter (of order 2) with the applied load in the calibration experiment performed to determine f_{σ} for sapphire. The linear scaling (red line) of the fringe diameter with load is evident. (b) Comparison of experimentally observed fringes and those reconstructed using Flamant's analytical solution for an elastic half-space subjected to a line load. Sapphire's plate thickness = 3 mm, 1,000 N load.

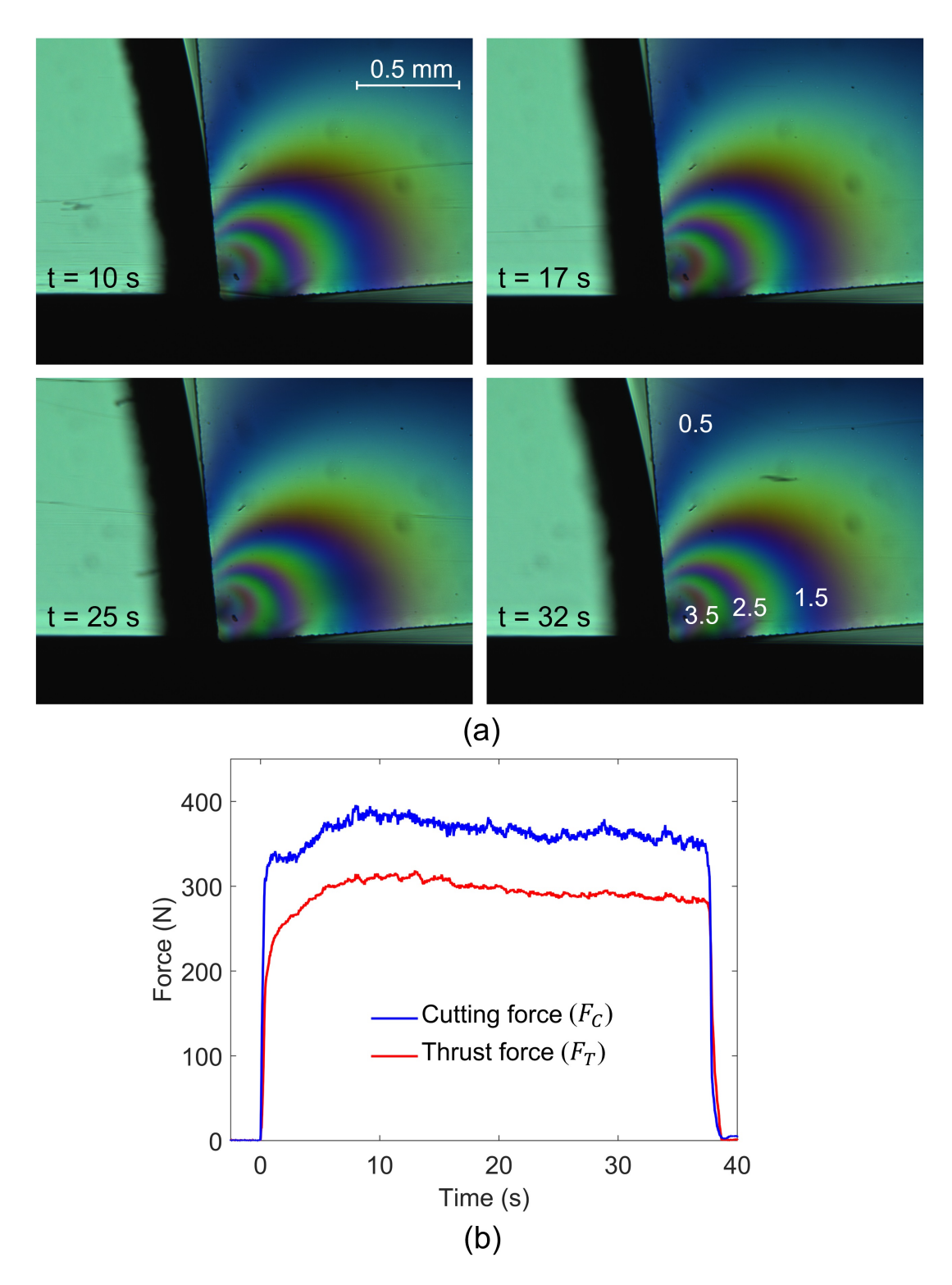


Figure 8: Stress state in cutting: (a) bright-field circular polariscope images taken at different time instances showing a stationary fringe pattern and steady-state nature of the cutting process; (b) cutting and thrust forces from a typical cutting experiment. The numbers in the bottom-right image in (a) represent the fringe order (N). Workpiece: brass, $t_0 = 40 \ \mu \text{m}$, $V_0 = 2 \ \text{mm/s}$, tool rake angle, $\alpha' = -5^{\circ}$.

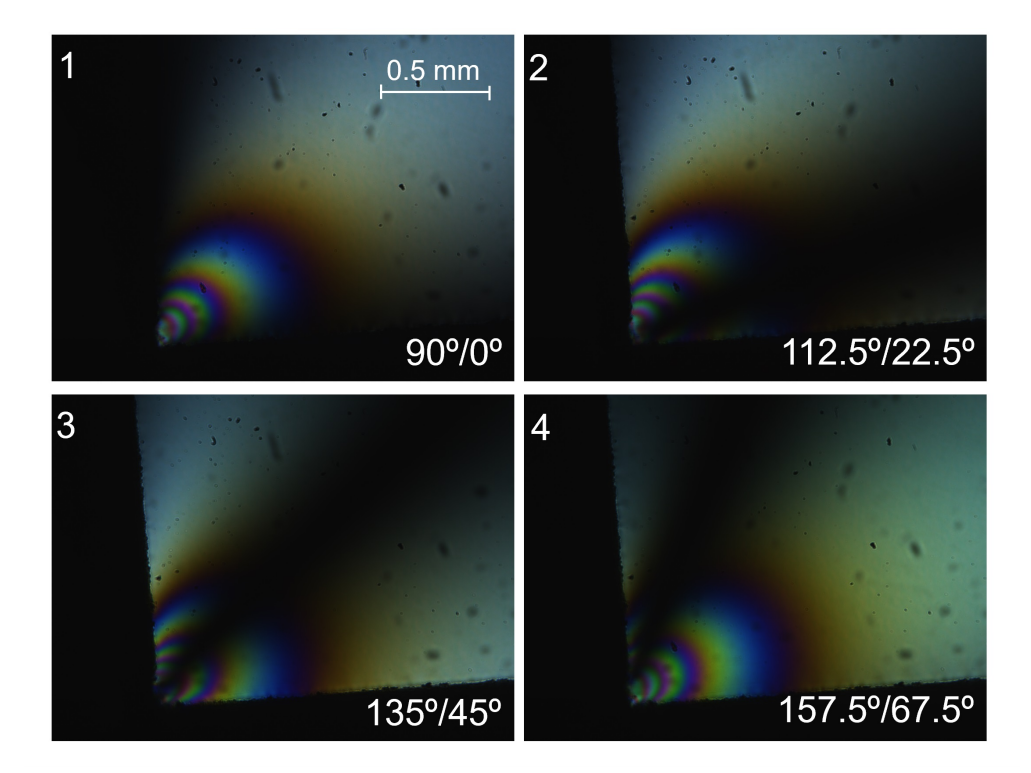


Figure 9: Images obtained using the plane polariscope arrangement (first four optical arrangements in the ten-step PST) while cutting brass. The angles represent the orientation of the polarizer and analyzer with respect to the horizontal direction, see Fig. 6 and Table 1. Note that the isoclinic fringe (black fringe) rotates with the polarizer and analyzer, while the isochromatic fringes (color fringes) remain stationary. $V_0 = 0.5 \text{ mm/s}$, $t_0 = 40 \ \mu\text{m}$.

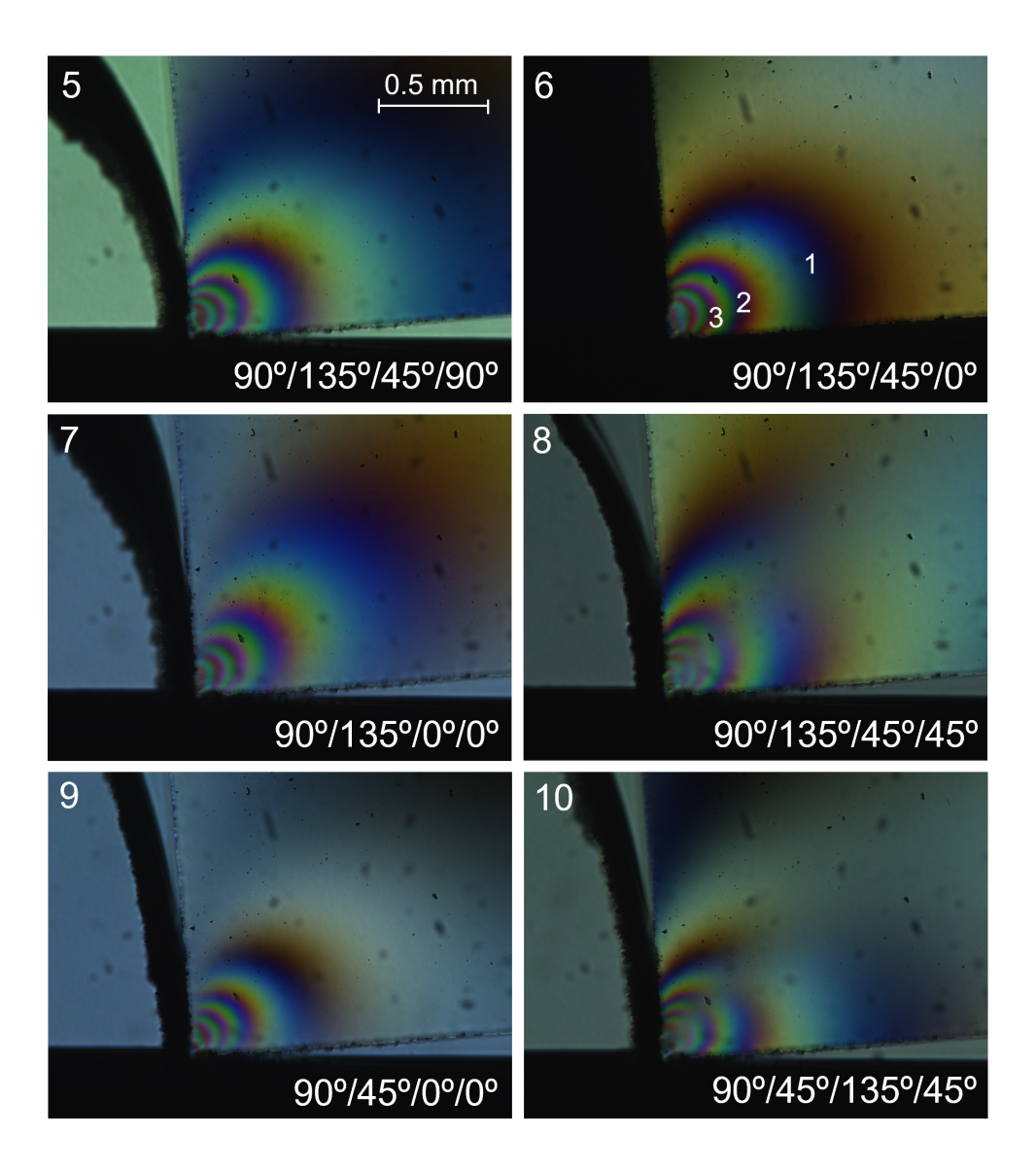


Figure 10: Images obtained using the circular polariscope arrangement (last six optical arrangements in the ten-step PST). The angles represent the orientation of the polarizer, first quarter-wave plate, second quarter-wave plate, and analyzer with respect to the horizontal, see Fig. 6 and Table 1. The first two images correspond to the conventional bright-field and dark-field circular polariscope arrangements, respectively.

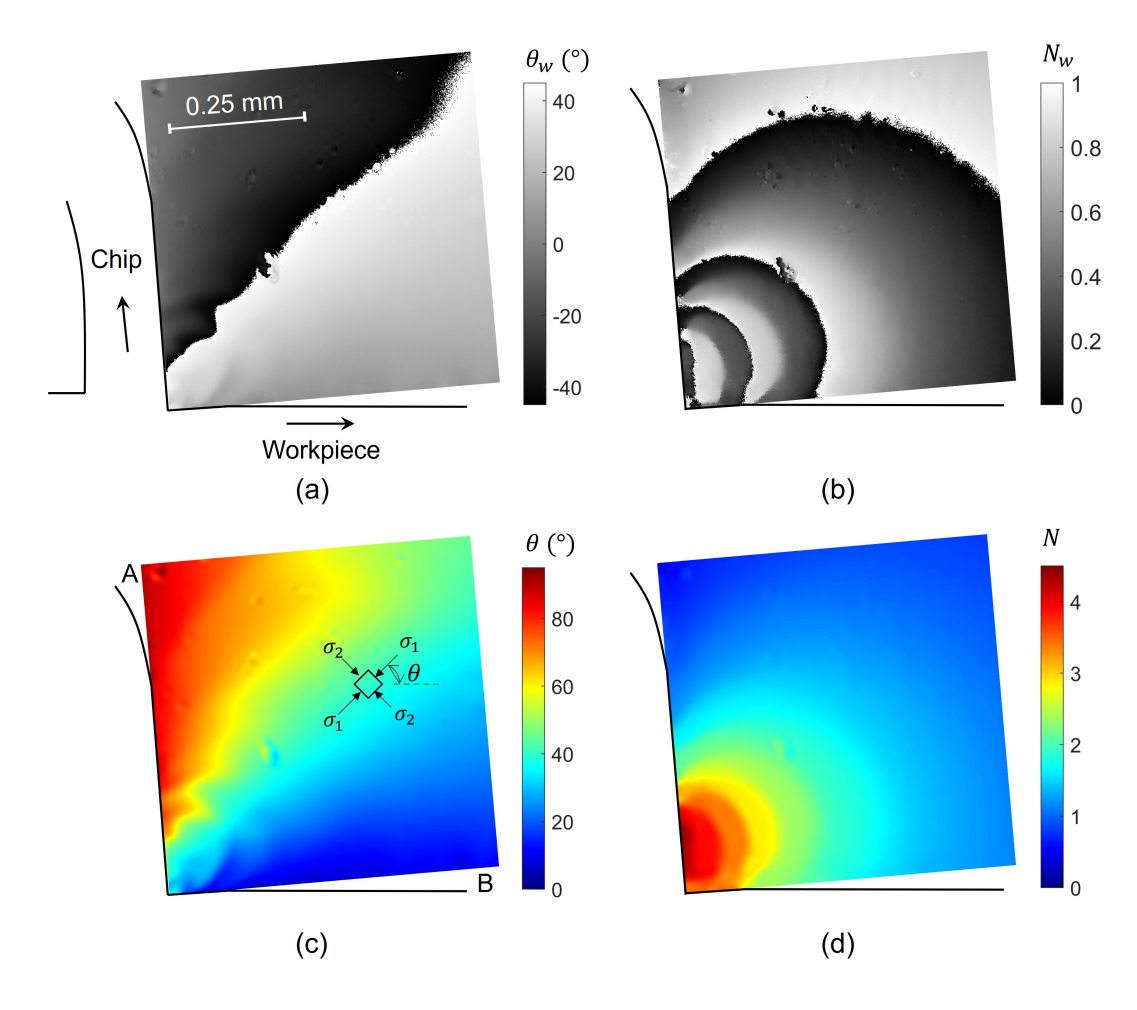


Figure 11: Isoclinic and isochromatic maps for cutting obtained using the ten-step PST and AQGPU algorithm: (a) wrapped isoclinic phase map (θ_w) , (b) wrapped isochromatic phase map (fractional fringe order, N_w), (c) unwrapped isoclinic phase map (principal stress direction, θ), and (d) unwrapped isochromatic phase map (fringe order, N). θ represents the angle of the largest principal stress with the horizontal. The principal stress difference can be obtained from the fringe order using the stress optics law.

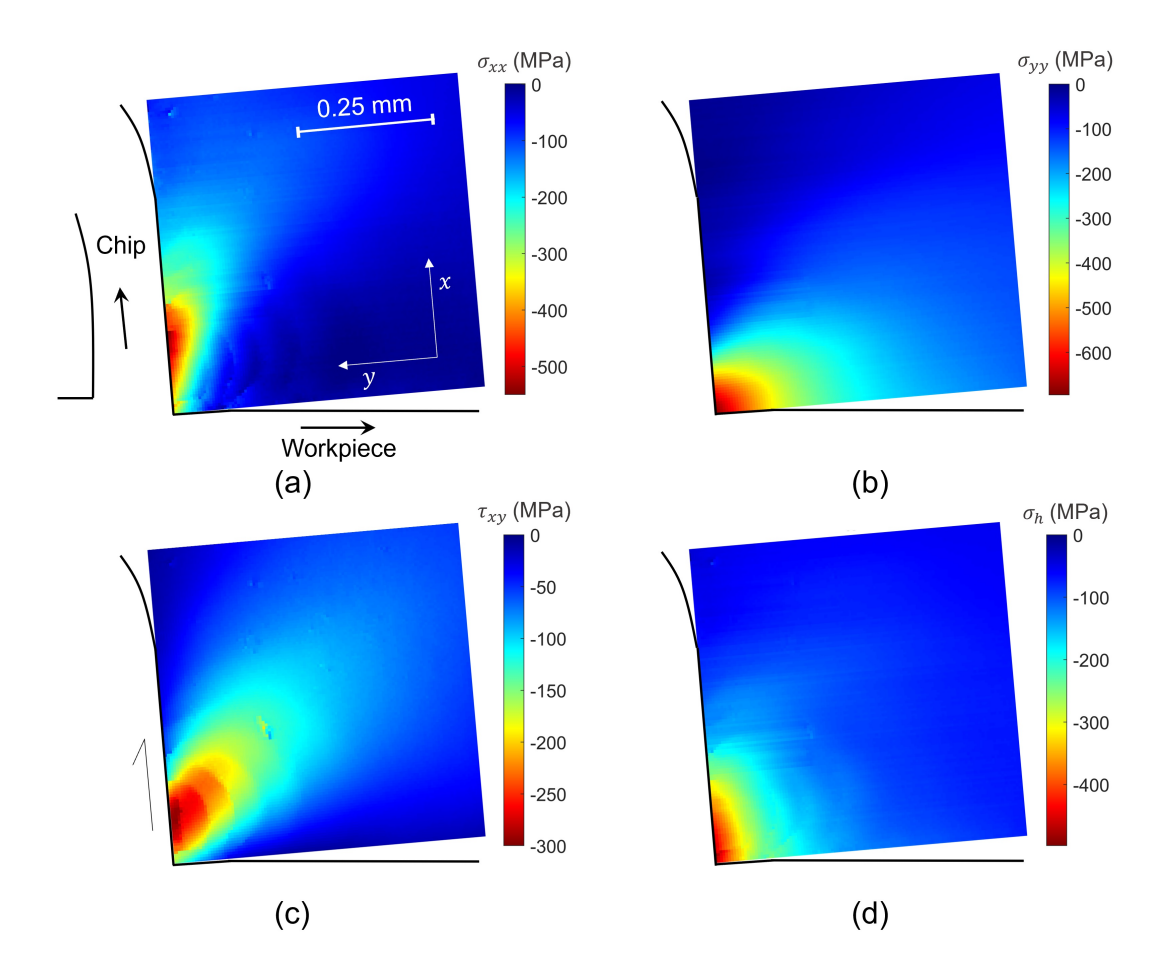


Figure 12: Full-field stress maps showing stress distribution in the cutting tool: (a) σ_{xx} (b) σ_{yy} , (c) τ_{xy} , and (d) σ_h (hyrdostatic stress). Note that the stress state is compressive, with the normal stress σ_{yy} (stress component normal to the rake face) showing a maximum at the tool tip. The shear stress τ_{xy} exhibits a maximum at some distance away from the tool tip along the rake face. See text for sign convention for the stresses.

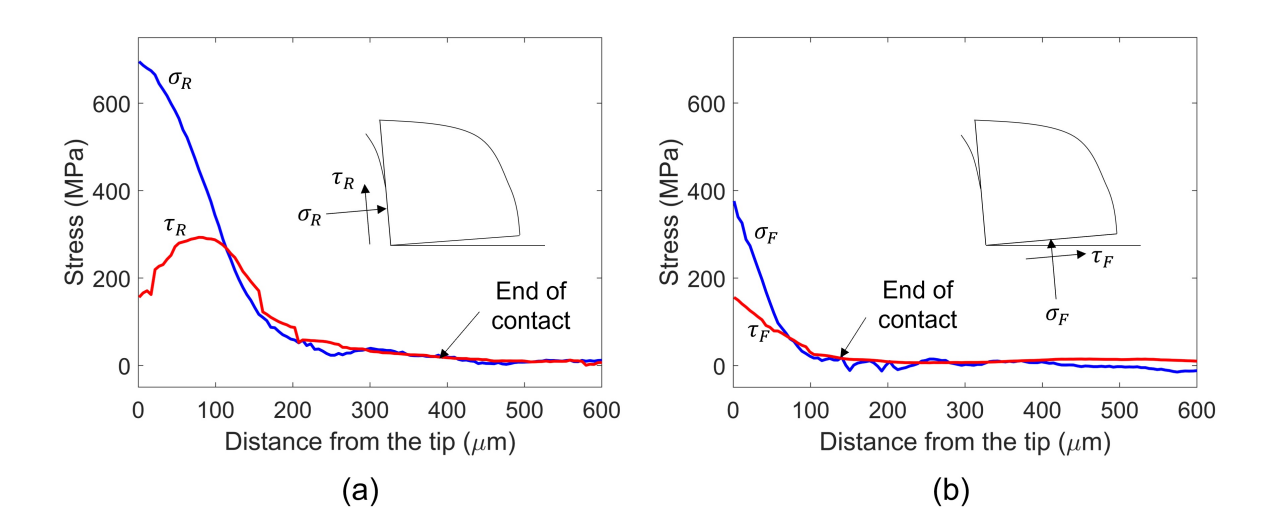


Figure 13: Contact normal (blue) and shear (red) stress profiles along the (a) rake face and (b) flank face of the cutting tool. Note the non-monotonic behavior of shear stress along the tool rake face in (a). σ_R and τ_R represent the normal and shear stresses along the rake face, while σ_F and τ_F are the corresponding normal and shear stresses along the flank face. In both cases, the normal stresses (σ_R and σ_F) are compressive.

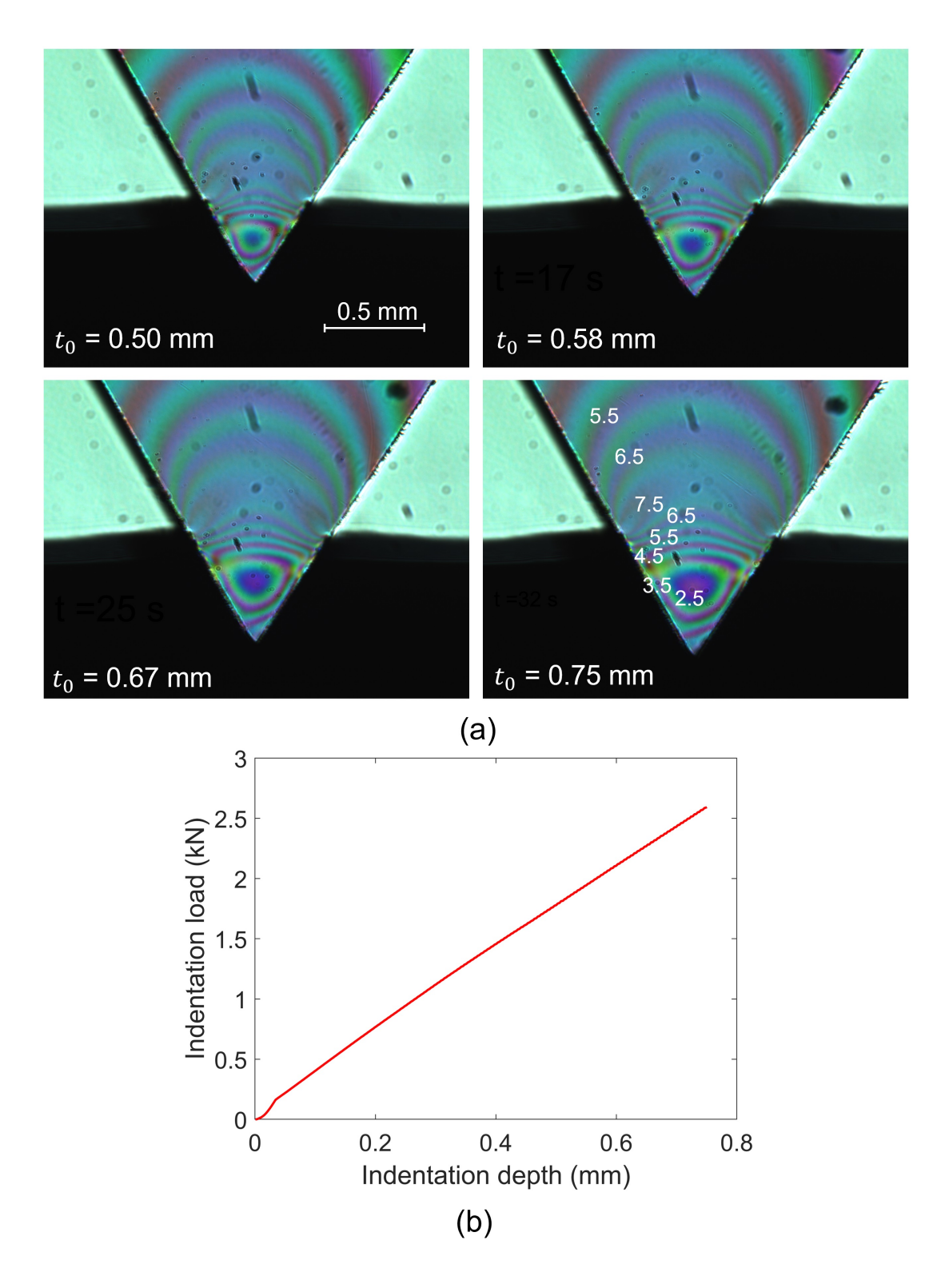


Figure 14: (a) Bright-field circular polariscope images at different depths of indentation (t_0) showing geometric similarity of the fringe contours. (b) Indentation load vs. depth data from the experiment. Workpiece: brass, indenter angle = 60° , indentation speed = 0.01 mm/s.

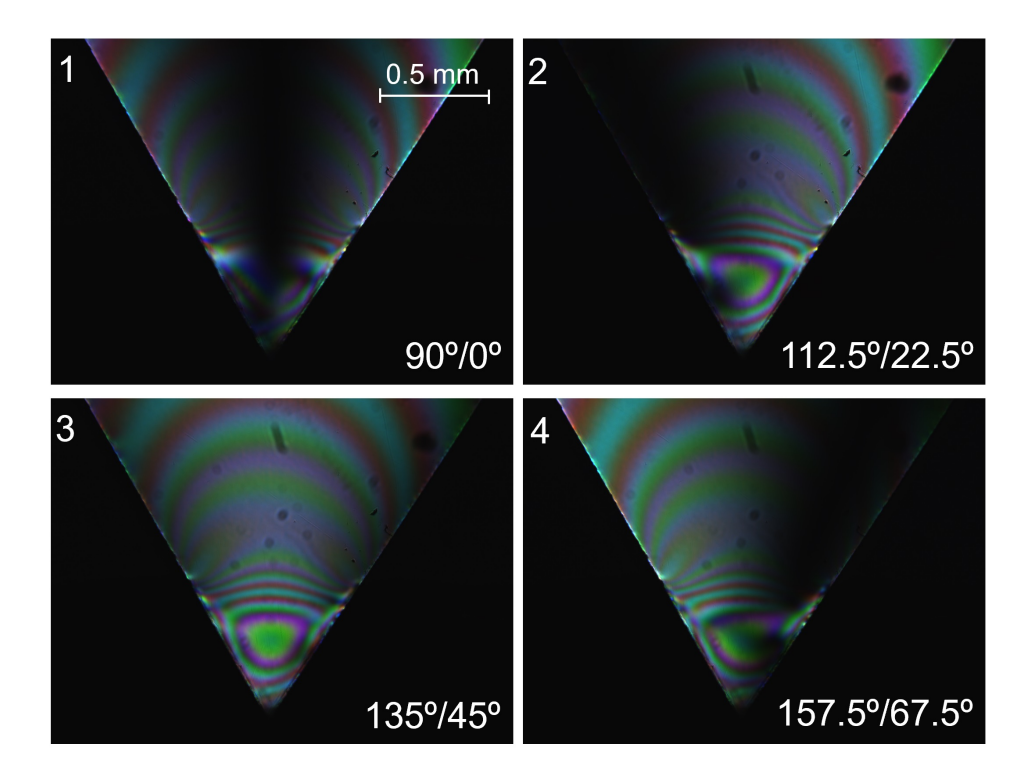


Figure 15: Images obtained using the plane polariscope arrangement (first four optical arrangements in the ten-step PST) at an indentation depth $t_0=0.75$ mm. The angles represent the orientation of the polarizer and analyzer with respect to the horizontal, see Fig. 6 and Table 1. Note the change in the isoclinic fringe (black fringe) location in the images, while the isochromatic fringes (color fringes) remain the same.

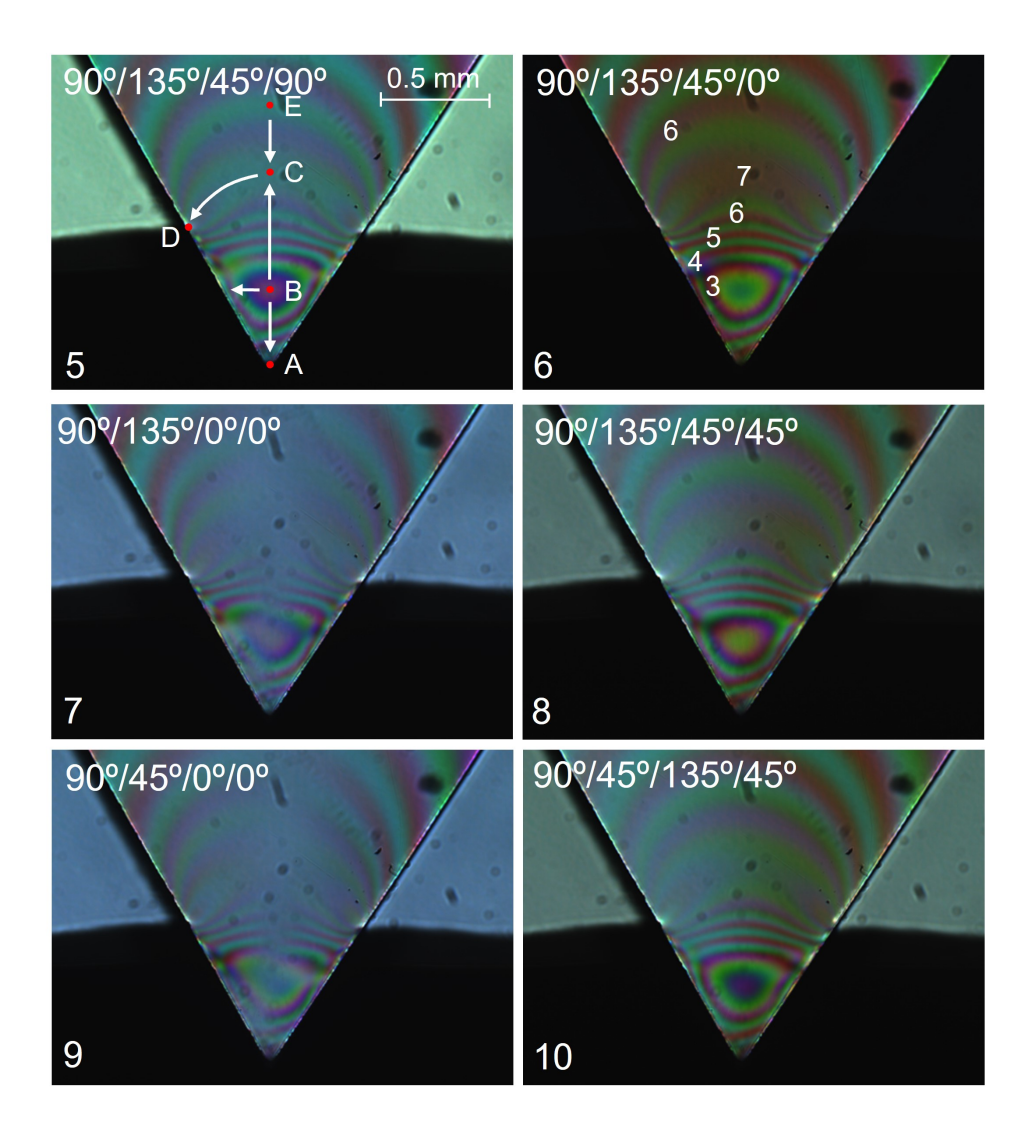


Figure 16: Images obtained using the circular polariscope arrangement (last six optical arrangements in the tenstep PST) at $t_0 = 0.75$ mm. The angles represent the orientation of the polarizer, first quarter-wave plate, second quarter-wave plate, and analyzer with respect to the horizontal, see Fig. 6 and Table 1. The arrows in the first image show the direction of increasing fringe order, see text for details on points A-E.

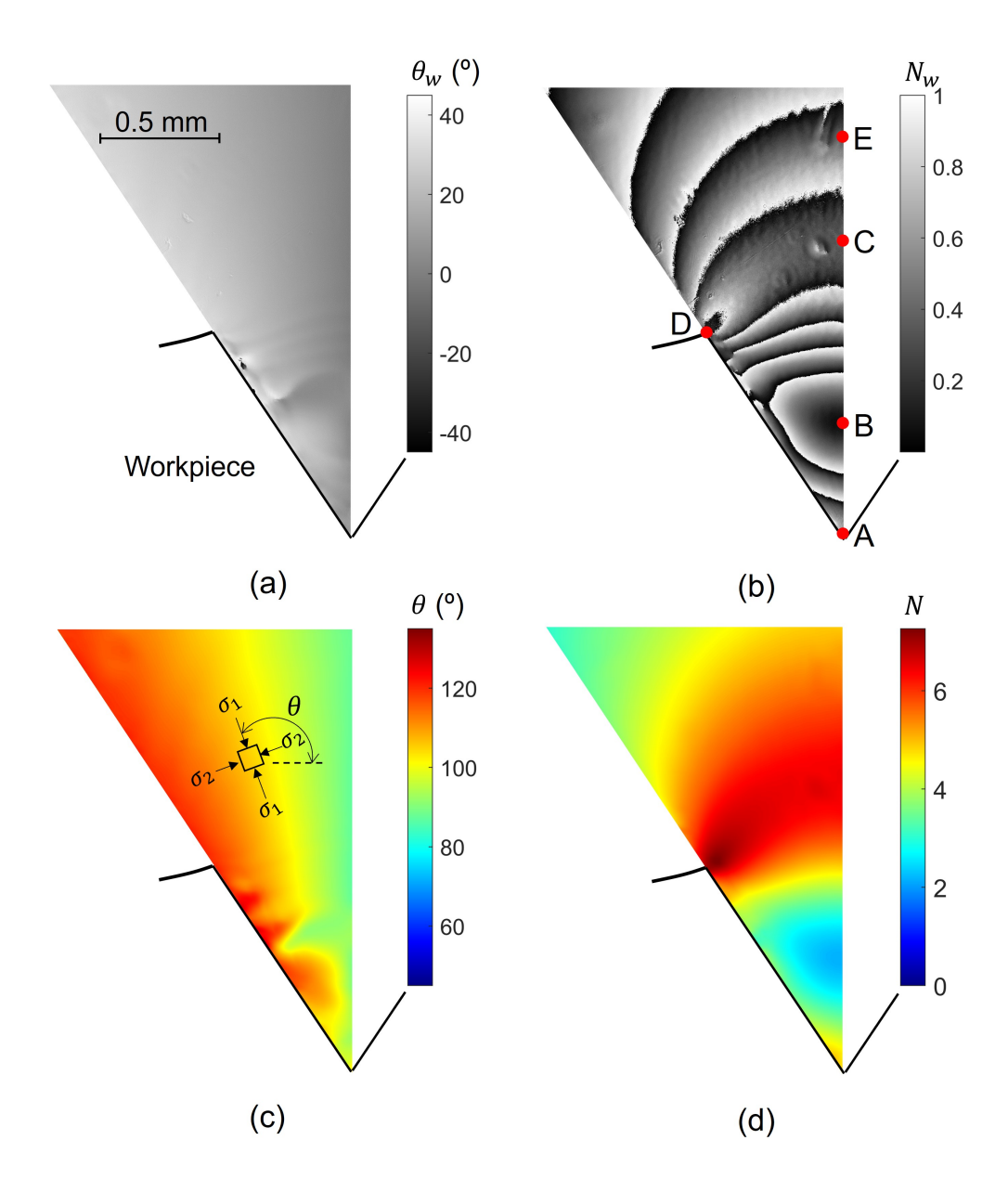


Figure 17: Isoclinic and isochromatic maps for wedge indentation obtained using the ten-step PST and AQGPU algorithm: (a) wrapped isoclinic phase map (θ_w) , (b) wrapped isochromatic phase map (fractional fringe order, N_w), (c) unwrapped isoclinic phase map (principal stress direction, θ), and (d) unwrapped isochromatic phase map (fringe order, N).

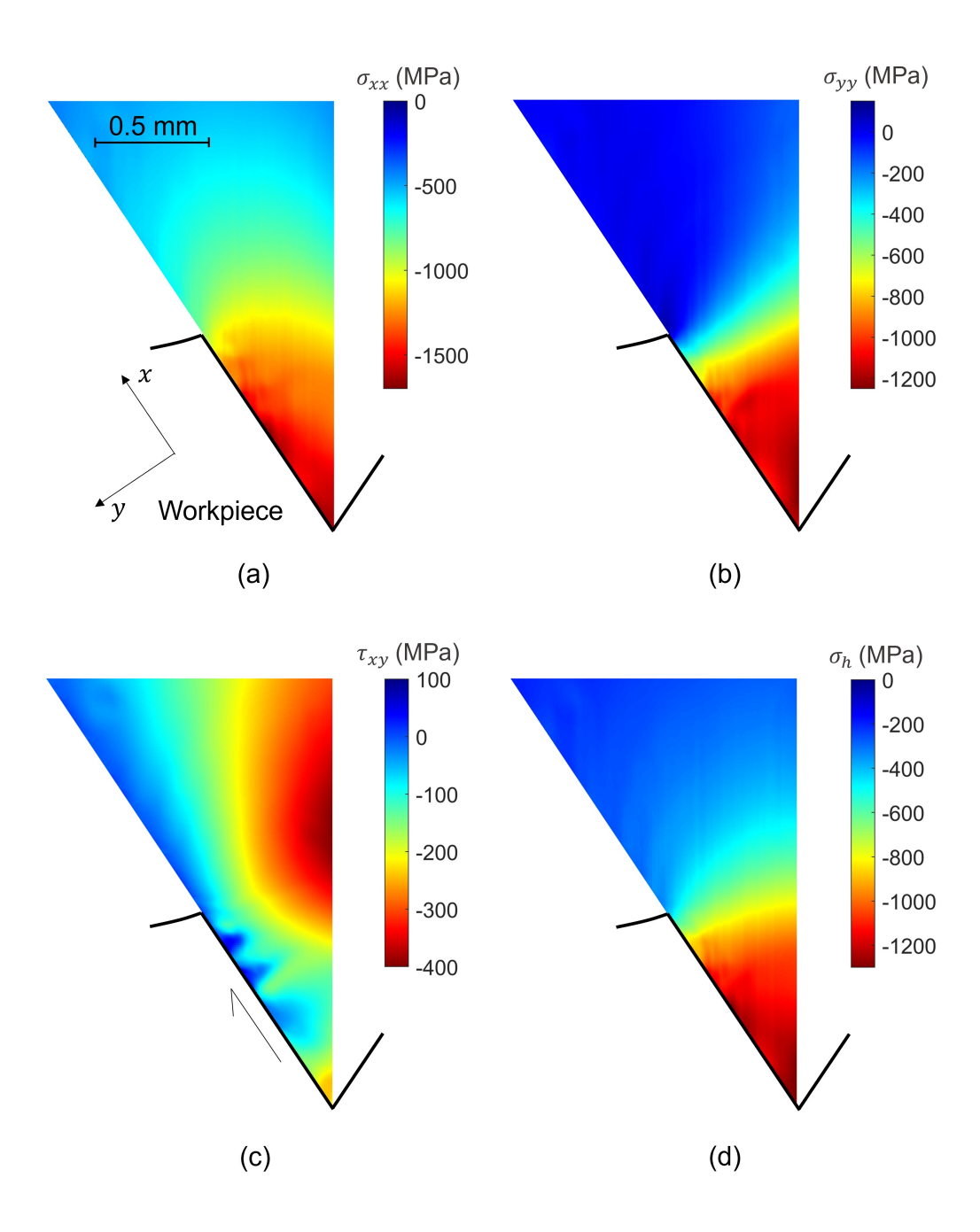


Figure 18: Full-field stress maps showing stress distribution in the indenter: (a) σ_{xx} (b) σ_{yy} , (c) τ_{xy} , and (d) σ_h (hydrostatic stress). Note the highly compressive stress state along the entire contact. τ_{xy} map in (c) also shows that the region near the indenter tip is also characterized by a high shear stress.

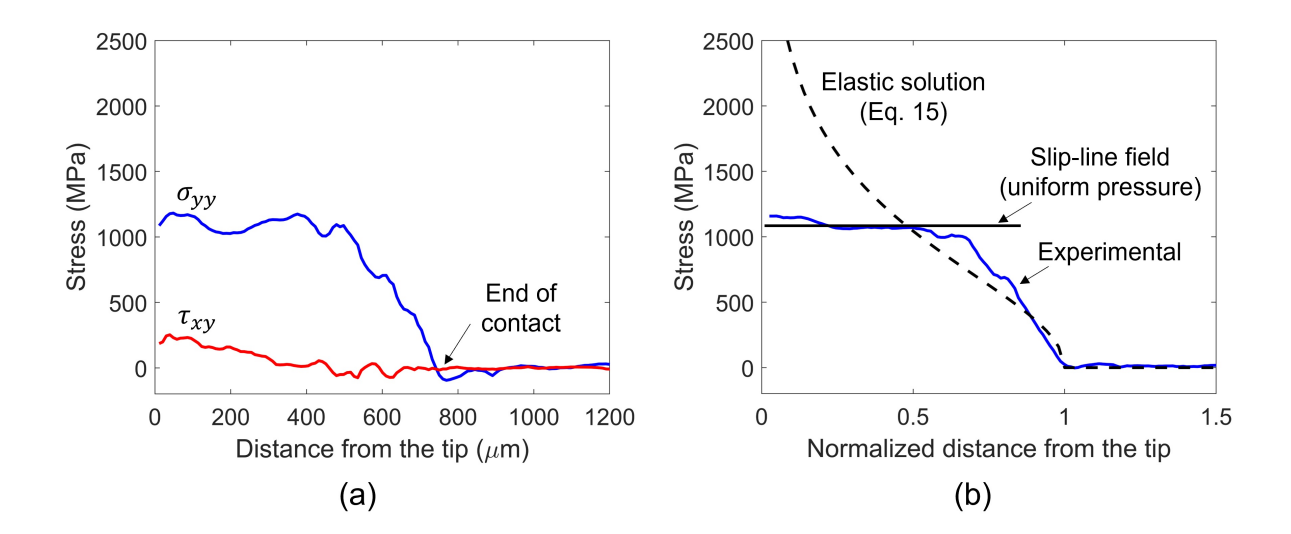


Figure 19: Contact stress profiles in wedge indentation. (a) Normal (blue) and shear (red) stress distribution along the indenter workpiece interface; the normal stress or interface pressure remains constant over $2/3^{\rm rd}$ s of the contact length, followed by a decay near the contact edge. (b) Comparison of experimentally observed pressure distribution (blue) with that predicted by slip-line field theory for a perfectly plastic material (uniform pressure, solid black line) and Sneddon's solution for wedge indentation of a perfectly elastic material (dashed black curve).

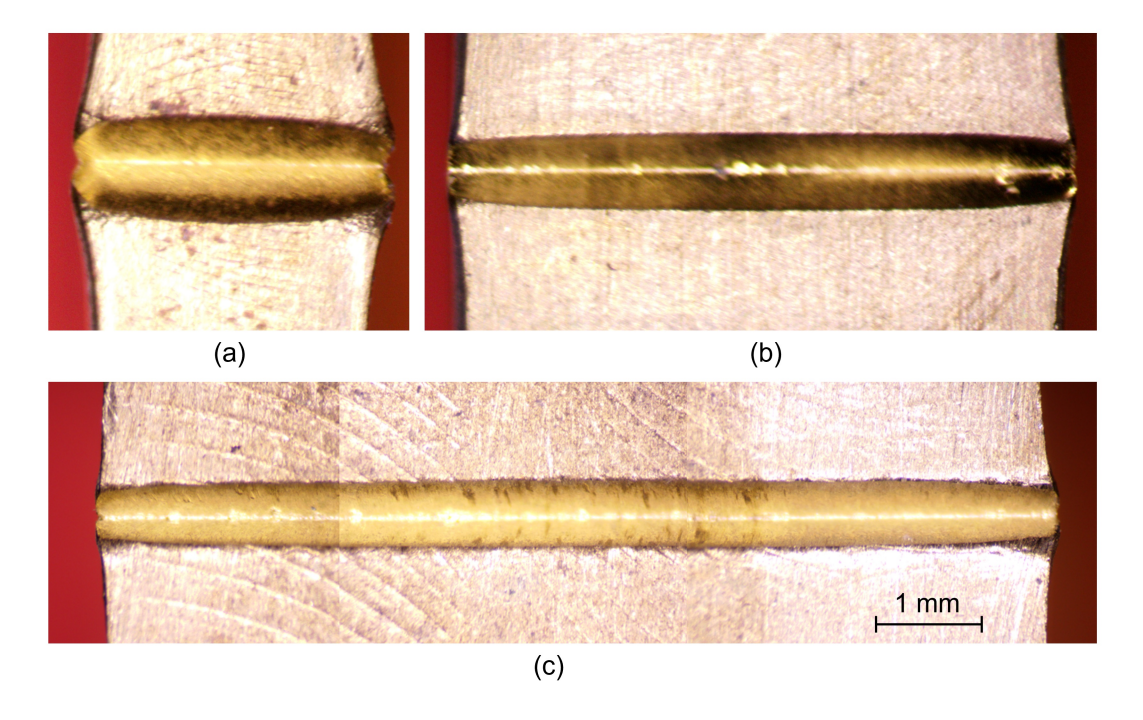


Figure A1: Images showing indentation tracks made under different w/t_0 ratios: (a) $w/t_0 = 4$, (b) $w/t_0 = 9$, and (c) $w/t_0 = 15$. Note the decrease in the lateral material flow at larger w/t_0 ratios.

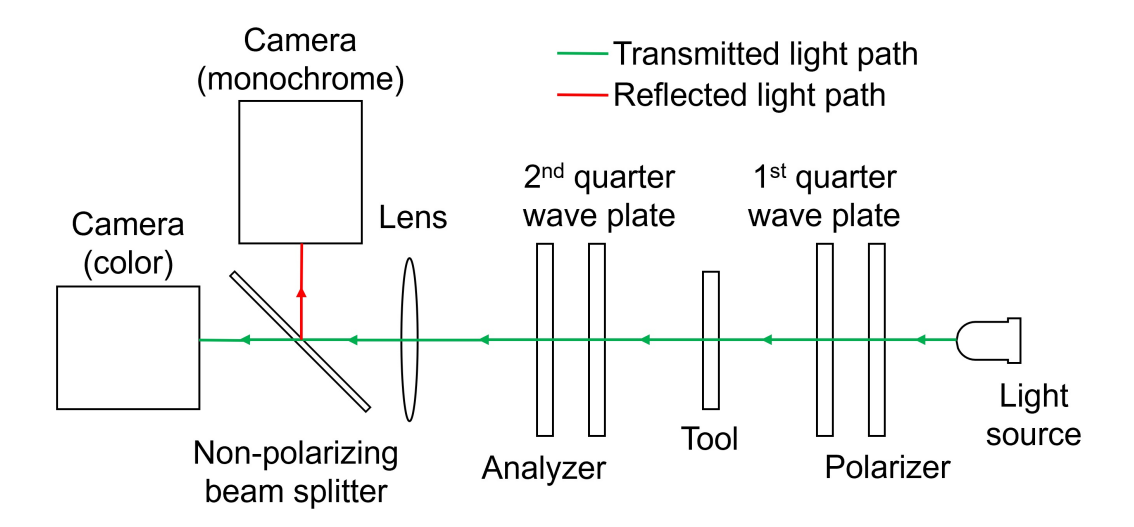


Figure A2: Schematic of the polariscope arrangement modified with a non-polarizing beam splitter to allow for image acquisition on two cameras simultaneously. The non-polarizing beam splitter splits the incoming light into two with a reflection/transmission ratio of 50/50 without altering the polarization state.

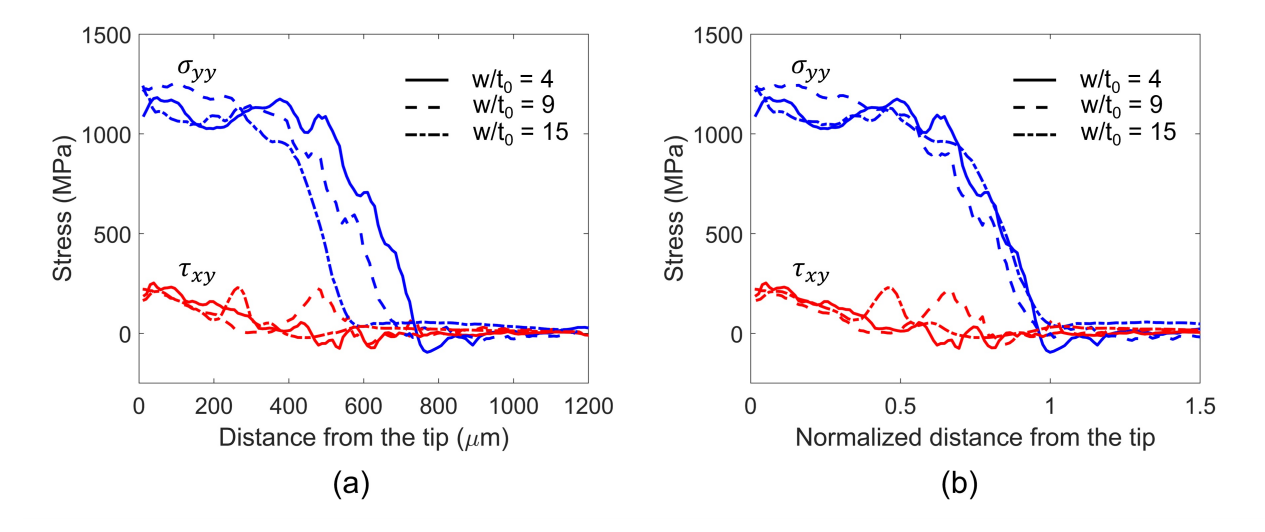


Figure A3: Contact stress profiles in wedge indentation. (a) Normal and shear stress profiles in indentation experiments with different w/t_0 ratios. In (b), the stresses are plotted against the normalized distance (i.e., distance from the indenter tip divided by the total contact length). The similarity in stress profiles in all the cases evident from the normalized plot.